Muthukrishnan *et al. BMC Medical Imaging* (2024) 24:182
https://doi.org/10.1186/s12880-024-01341-1

BMC Medical Imaging

RESEARCH **Open Access**

Continuum topological derivative - a novel application tool for denoising CT and MRI medical images

Viswanath Muthukrishnan[1], Sandeep Jaipurkar[2] and Nedumaran Damodaran[1*]

Abstract

Background CT and MRI modalities are important diagnostics tools for exploring the anatomical and tissue properties, respectively of the human beings. Several advancements like HRCT, FLAIR and Propeller have advantages in diagnosing the diseases very accurately, but still have enough space for improvements due to the presence of inherent and instrument noises. In the case of CT and MRI, the quantum mottle and the Gaussian and Rayleigh noises, respectively are still present in their advanced modalities of imaging. This paper addresses the denoising problem with continuum topological derivative technique and proved its trustworthiness based on the comparative study with other traditional filtration methods such as spatial, adaptive, frequency and transformation techniques using measures like visual inspection and performance metrics.

Methods This research study focuses on identifying a novel method for denoising by testing different filters on HRCT (High-Resolution Computed Tomography) and MR (Magnetic Resonance) images. The images were acquired from the Image Art Radiological Scan Centre using the SOMATOM CT and SIGNA Explorer (operating at 1.5 Tesla) machines. To compare the performance of the proposed CTD (Continuum Topological Derivative) method, various filters were tested on both HRCT and MR images. The filters tested for comparison were Gaussian (2D convolution operator), Wiener (deconvolution operator), Laplacian and Laplacian diagonal (2nd order partial differential operator), Average, Minimum, and Median (ordinary spatial operators), PMAD (Anisotropic diffusion operator), Kuan (statistical operator), Frost (exponential convolution operator), and HAAR Wavelet (time–frequency operator). The purpose of the study was to evaluate the effectiveness of the CTD method in removing noise compared to the other filters. The performance metrics were analyzed to assess the diligence of noise removal achieved by the CTD method. The primary outcome of the study was the removal of quantum mottle noise in HRCT images, while the secondary outcome focused on removing Gaussian (foreground) and Rayleigh (background) noise in MR images. The study aimed to observe the dynamics of noise removal by examining the values of the performance metrics.

In summary, this study aimed to assess the denoising ability of various filters in HRCT and MR images, with the CTD method being the proposed approach. The study evaluated the performance of each filter using specific metrics and compared the results to determine the effectiveness of the CTD method in removing noise from the images.

Results Based on the calculated performance metric values, it has been observed that the CTD method successfully removed quantum mottle noise in HRCT images and Gaussian as well as Rayleigh noise in MRI. This can be evidenced by the PSNR (Peak Signal-to-Noise Ratio) metric, which consistently exhibited values ranging from 50 to 65 for all

---

*Correspondence:
Nedumaran Damodaran
dnmaran@gmail.com
Full list of author information is available at the end of the article

© The Author(s) 2024. **Open Access** This article is licensed under a Creative Commons Attribution 4.0 International License, which permits use, sharing, adaptation, distribution and reproduction in any medium or format, as long as you give appropriate credit to the original author(s) and the source, provide a link to the Creative Commons licence, and indicate if changes were made. The images or other third party material in this article are included in the article's Creative Commons licence, unless indicated otherwise in a credit line to the material. If material is not included in the article's Creative Commons licence and your intended use is not permitted by statutory regulation or exceeds the permitted use, you will need to obtain permission directly from the copyright holder. To view a copy of this licence, visit http://creativecommons.org/licenses/by/4.0/. The Creative Commons Public Domain Dedication waiver (http://creativecommons.org/publicdomain/zero/1.0/) applies to the data made available in this article, unless otherwise stated in a credit line to the data.

the tested images. Additionally, the CTD method demonstrated remarkably low residual values, typically on the order of e^{-09}, which is a distinctive characteristic across all the images. Furthermore, the performance metrics of the CTD method consistently outperformed those of the other tested methods. Consequently, the results of this study have significant implications for the quality, structural similarity, and contrast of HRCT and MR images, enabling clinicians to obtain finer details for diagnostic purposes.

Conclusion Continuum topological derivative algorithm is found to be constructive in removing prominent noises in both CT and MRI images and can serve as a potential tool for recognition of anatomical details in case of diseased and normal ones. The results obtained from this research work are highly inspiring and offer great promise in obtaining accurate diagnostic information for critical cases such as Thoracic Cavity Carina, Brain SPI Globe Lens 4th Ventricle, Brain-Middle Cerebral Artery, Brain-Middle Cerebral Artery and neoplastic lesions. These findings lay the foundation for implementing the proposed CTD technique in routine clinical diagnosis.

Keywords Denoising, Continuum topological derivative, HRCT images, MRI images, Quantum mottle, Rayleigh noise, Gaussian noise

Introduction

Medical imaging technology have been grown rapidly from the screen-film to the sophisticated medical images arising from modern modalities wherein digital imaging have been playing a predominant role, in particular CT and MRI. Medical image analysis is aided by various image processing tools like image enhancement, quantification, visualization and computer aided detection [1, 2]. Objective of image restoration is denoising of the degraded medical image to remove the noise generated from non-linearity of sensors, grains, defects in image capturing, erroneous focus of image, distortion due to relative motion of object during imaging, etc.

Imaging modalities

In this paper, two imaging modalities such as CT and MRI and their denoising characteristics using CTD technique are presented.

Computer Tomography (CT)

Computer Tomography (CT) has been developed in stages like planar, cross-section and 3-D reconstruction, etc., and has attained the present stage of High Resolution Computed Tomography (HRCT) [3–7]. In HRCT, minimum field of view and optimized resolution of images are the main highlights of HRCT, which proved its ability to give clear images to find lung fibrosis [8], and bronchial tree lesion [9–11]. Further, the image reconstruction algorithms employed in HRCT are capable of extending high spatial-frequency resolution.

Since its introduction in 1972, computed tomography (CT) has evolved significantly with advancements including cardiac gating CT, spectral CT, multidetector CT (MDCT), energy-sensitive photon counting detector CT (PCD-CT), phase contrast CT, spiral CT, sequential CT, coronary CT, triple-phase CT, electron beam CT (EBCT), helical CT, perfusion CT, and high-resolution CT (HRCT), among others. The utilization of SOMATOM HRCT in this study offers several advantages. It allows for low contrast agent dosage, as X-ray tubes can generate high mA at low kV even with reduced contrast agent usage. Additionally, it minimizes the use of rare earth metals and incorporates a high number of detectors, resulting in energy-efficient HRCT machines. This is particularly beneficial for thorax and cardiac procedures, as it facilitates dynamic imaging with excellent temporal resolution, fast scan results, accurate neuro perfusion maps, and reduced metal and motion artifacts. HRCT proves to be highly valuable in the diagnosis of lung disorders and diseases within the thorax region due to its exceptional accuracy.

Magnetic Resonance Imaging (MRI)

In Magnetic Resonance Imaging (MRI), radio wave is applied on the human beings (excitation or protons) under the influence of strong magnetic field (to align the precision of the proton in a particular direction of the applied magnetic field) and detecting the relaxation times like T1 and T2 of the excited protons forms the basis of the MRI. For image formation in MRI, Radon transform or Fourier Transform was employed [12] to convert the k-space proton relaxation time into pixels. The MRI advanced modalities like Fluid Attenuated Inversion Recovery (FLAIR), Diffusion Weighed Imaging (DWI), and Periodically Rotated Overlapping Parallel Lines with Enhanced Reconstruction (PROPELLER) have helped to overcome the MRI sample *k-space* over a rotatory time period.

In the case of MRI, the three principal nuclei utilized to study metabolism, fluids, and cell membrane composition with pH levels are carbon (C-13), hydrogen, and phosphorus (P31), respectively. For this research, the SIGNA Explore MRI machine was employed, which offers several advantages. It provides very silent scans (< 3 decibels), enables 3D volumetric brain imaging, allows for free-breathing scans, facilitates low sedation scans, distinguishes between calcifications and blood vessels effectively, and provides good proton density sequences. These features enhance the overall imaging experience and contribute to obtaining high-quality results in terms of noise reduction, precise volumetric imaging, and accurate differentiation between different tissues and structures.

Noises in CT and MR images

In this work, two different types of noises originating from the CT and MRI are attempted using the proposed CTD algorithm.

Quantum mottle in CT

Quantum mottle is one of the preliminary noises in CT due to loss in photon reaching the detector, which causes image density fluctuation, decreased spatial resolution and poor contrast resolution. This loss in the number of photons is governed by the Poisson distribution on a pixel-to-pixel scale. If $P^{avg}_{/p}$ is the average number of photons per pixel then, the standard deviation can be defined as $P^{SD}_{avg} = \sqrt{P^{avg}_{/p}}$. Now the observed quantum mottle noise Q^{CT}_N can be equated as

$$Q^{CT}_N = \sqrt{P^{SD}_{avg}} \Big/ P^{avg}_{/p} \tag{1}$$

In the above Eq. (1), Q^{CT}_N is the distributive noise. For quantum noise removal, Filtered Back Projection (FBP) and sinogram affirmed iterative reconstruction (SAFIRE) techniques were used for the estimation of quantum noise in CT images [13–17]. Wavelet transform and its different modes and types were experimented for removing the quantum mottle noise in CT [18–24]. Further, spatio-temporal filtering [25], Bayes filter [26], multineural network filter [27], adaptive multineural network filter [28], stochastic method [29], adaptive statistical iterative reconstruction-V [30], iterative reconstruction algorithm [31–36], deep learning reconstruction algorithm [37, 38], Shearlet transform [39] and neural network [16] are some of the other methods tried to reduce the quantum mottle noise in CT images. The denoising process in the wavelet method involves decomposition of levels, thresholding, and scaling factors. Spatio-temporal filtering, on the other hand, utilizes ordinary mathematical operations followed by basic statistical operations. However, these approaches often struggle to produce crucial diagnostic information due to the averaging of image contents.

In contrast, the Bayes filter employs probability density functions for the filtering process, while neural, multineural, and adaptive multineural methods are based on training datasets. Adaptive statistical iterative reconstruction utilizes statistical and probability distribution functions to perform the filtering operation. The Shearlet transform, on the other hand, utilizes sparse representation to denoise quantum mottle noise.

While these methods often involve averaging existing information through mathematical operations or require time-consuming iterative algorithm testing, the proposed CTD method takes a different approach. It applies a simple perturbation (cost-function) threshold to identify noise information from useful pixel information. This allows for accurate details by discarding the noise information as desired. Moreover, the cost-function can be adjusted to fine-tune the denoising process and obtain precise results [40–51].

Gaussian and Rayleigh's noises in MRI

In MRI, k-space variables are used to form the image using Radon transformation. Noise in $k-space$ is characterised by independent and identically distributed random variables called, Gaussian Random variables, which are complex in nature. In MRI, feature extraction and classification are affected by these noises and are additive in nature. Various researchers have tried to reduce the noises in MRI using different filtering techniques [52–55].

The Gaussian noise present in MRI image [56] can be expressed as

$$N^{G}_{MRI} = \sqrt{D^{rs}_{MRI} N^{G1}_{MRI}} + N^{G2}_{MRI} \tag{2}$$

In the above Eq. (2), N^{G}_{MRI} represents the Gaussian noise of the MRI image, N^{G1}_{MRI} and N^{G2}_{MRI} are independent zero-means. Wavelet filters [57–61], histogram equalization [62, 63], median filter [64–67] total variation method [55], adaptive wiener filter [68], multiscale enhancement along with Susan edge detector [69], Bayesian method [70], non-local means filter [71, 72], hybrid adaptive algorithm [66], anisotropic diffusion filter [40, 41, 73], bilateral filter [74], convolution neural network [75] and non-local averaging [42] are some of the techniques employed for denoising the Gaussian noise in MRI images. When it comes to Gaussian noise present in MR images, different denoising methods exhibit varying strengths. Histogram equalization primarily enhances contrast information, while the total variation method, multiscale enhancement, and bilateral filters excel in preserving sharp edges. The Bayesian approach can remove additive white noise in MRI, but its effectiveness may be limited. Non-Local Means (NLM) and hybrid adaptive algorithms are often successful in reducing random noise in MRI. On the other hand, the anisotropic diffusion filter and non-local averaging methods can only moderately reduce Gaussian noise in MR images. It is important to note that no single method is capable of reducing Gaussian noise to the desired level perfectly.

Therefore, the proposed CTD method was implemented to address noise reduction in a constructive manner, considering the limitations of other methods. By employing a tailored approach, the CTD method aims to effectively reduce noise while preserving important image details [65, 76–81].

Rayleigh noise concentrates on the magnitude of the image and lies in the background of the MRI image. This background noise removal brings down the lossless compression ratio, which improve the efficiency of image transfer through internet for telemedicine purposes [43]. Rayleigh noise depends on the noise density in the image pixels and is modelled on the Rayleigh curve represented by

$$N_d^{Ry}\left(I_m^g\right) = \begin{bmatrix} \frac{2}{g_1}[g - g_0]e^{\frac{(g-g_0)^2}{g_1}} & g \geq g_0 \\ 0 & g < g_0 \end{bmatrix} \quad (3)$$

In Eq. (3), $N_d^{Ry}\left(I_m^g\right)$ gives the noise density, g represents the grey level intensity, g_0 represents the minimum grey level intensity and g_1 represents the maximum grey level intensity.

Haar wavelet [43], complex diffusion prior [44], partial differential equation [45, 82, 83], Villullas-Martin's filter [46], anisotropic diffusion [47], adaptive filters [48], discrete complex wavelet [49], Taylor-Krill Herd-based Support Vector Machine [50], Bayes classifier [51], conventional approach [84], maximum-likelihood [85], orthogonal matching pursuit sparsity method [86], genetic programming [87], Markov random fields based maximum a posteriori method [88], non-linear regression models [89], sum of squares reconstruction [90], Bayesian [91], variational model [92], non-local mean filter [72], multi-dilated block network [76] and Nakagami distribution [77] were deployed to remove the Rayleigh noise in MRI images. While these methods were able to reduce Rayleigh noise to a moderate level, the Villullas-Martin's filter fell short in preserving contour details as expected. The maximum-likelihood method focused solely on removing thermal noise in MRI, and the orthogonal matching pursuit sparsity method only provided a solution for sparse representation.

In order to address the limitations and drawbacks of these existing methods for removing Rayleigh noise in MRI, the proposed CTD method was implemented. The CTD method aims to overcome these limitations by offering improved noise reduction while preserving contour details to the desired level [93–102].

Methodology

Denoising filters have wide applications in removing the noises present in most of the imaging modalities. They can be categorized as spatial [65, 78–81, 103–105], adaptive [106, 107] and transformation [108] filters. Spatial filters are classified into linear and non-linear types concentrating on neighbourhood operations. Adaptive filters operate on statistical measures like mean and variance, while the transformation filters depend on techniques like Fourier, Curvelet, Contourlet and Wavelet transforms. Filters along with their functions are summarized in Table 1. These noise filters were tested for noise removal in CT and MR images and their performance are summarized in Table 1. These three different categories of traditional filter have been chosen for this work for estimating the performance of the proposed CTD filter by comparing their denoising characteristics using various performance measures. For comparing the performance of the filters, eighteen performance metrics viz., Average Difference (AD), Mean Square Error (MSE), Root Mean Square Error (RMSE), Maximum Difference (MD), Normalized Absolute Error (NAE) and Normalized Mean Square Error (NMSE), Peak Signal to Noise Ratio (PSNR), Structural Content (SC), Correlation Coefficient (CC), Normalized Cross Correlation (NCC), Image Quality Index (IQI) and Structural Similarity Index Map (SSIM), Contrast to Noise Ratio (CNR), Noise Index (NI), Average Signal to Noise Ratio (ASNR), Image Variance (IV), Noise Standard Deviation (NSD), and Equivalent Number of Looks (ENL) were selected and their mathematical forms, definition and range of values are summarized in Table 2 [109].

The proposed CTD filter and its mathematical definition are described in the following section.

Continuum Topological Derivative (CTD)

The Topological Derivative (TD) concept was originally conceived from structural mechanics to solve shape optimization and topology optimization problems. Later on, it was utilized to solve image processing problems. In this research work, Continuum Topological Derivative (CTD) was proposed for solving discontinuities in the domain, boundaries and improving the shape sensitivity of CT and MR images [110].

Further, the CTD can be effective in solving the changes occurred during processing of images. All these features of the CTD impressed us to choose for denoising the CT and MR images. The main advantage of CTD lies

Table 1 List of de-noising filters used

Name	Type	Mathematical function	Resultant Image	Noise Removal
Gaussian	Frequency	Cut off	Smooth	Average
Wiener	Frequency	Low pass	Smooth	Better
Laplacian	Linear	Derivative	Edge detection	Average
Laplacian Diagonal	Linear	Derivative	Sharp	Poor
Average	Spatial (Low pass)	Average	Blurred Edges	Average
Minimum	Non-linear	Minimum	Smooth	Poor
Median	Non-linear	Medium	Smooth	Good
PMAD	Diffusion	Derivative	Smooth	Average
Kuan	Adaptive	Statistical	Smooth	Good
Frost	Adaptive	Statistical	Smooth	Good
HAAR Wavelet	Frequency	Orthogonal	Smooth	Very Good
CTD	Isotropic Conductivity Diffusion	Cost	High quality & contrast denoised image	Superlative

that even after the object got distorted by an external factor, it is still possible to study the properties of the object with respect to the original one [111]. This concept further influences the proposed denoising studies carried out in CT and MR images [112]. The topological derivative can be expressed as,

$$D_T(\widehat{x}) = \lim_{\varepsilon \to \infty} \frac{\Psi(\Omega_\varepsilon) - \Psi(\Omega)}{f(\varepsilon)} \tag{4}$$

where $\Psi(\Omega_\varepsilon)$ is the cost function of the perturbed domain, $\Psi(\Omega)$ is the cost function of the original domain, $f(\varepsilon)$ is the monotone function, $D_T(\widehat{x})$ is the topological derivative for a perturbation factor ε. Further, TD with advanced techniques like wavelet transform, Discrete Filter Bank (DFB), and Contourlet Transform (CLT) have been experimented to solve the perturbed domain issues of extracting contours, boundaries and edges in biomedical images [93]. The TD, CLT and interpolation methods help to resolve the edges in the organs of the biomedical images [94]. The CLT with Pyramidal Directional Filter Bank (PDFB) acts as a tool for flexibility of decomposition at the sub-band level [95]. The TD can produce enhanced efficiency in the segmentation of medical images with the introduction of diffusion concept [96]. Moreover, the Topological derivative could be applied for getting resolved images in Electrical Impedance Tomography (EIT) [97]. The TD with functional analysis techniques can provide emphasized results in delineation attributes of the medical images [98]. In the case of Continuum Topological Derivative (CTD), the features like shape functional, asymptotic expansion, sensitivity, and boundary and edge functional play a pivotal role in CTD while arriving at denoising results of CT and MRI medical images. The fundamental expression for CTD is given by,

$$\Psi[\Omega_\varepsilon] - \Psi[\Omega] = f_\varepsilon D_C^T(\hat{x}) \tag{5}$$

The Eq. (5) lays the foundation stone for CTD expressed in terms of cost function of original and perturbed domains along with monotonic function. Treating the state equation as the domain, which represents a specific region in the human body or an specific organ in the human body, the shape of it will be represented as $\Psi[\Omega]$, where Ψ is the state function and the Ω is the domain that is characteristic of the state equation. Here, $\Psi[\Omega]$ handles the original domain in an undisturbed state. Introduction of a perturbation into this domain will induce topological variation in the state of the domain. In such a case, $\Psi[\Omega]$ is defined by the approximate solution. Obtaining approximate solution to linear system in the case of sparse system provides a perceptual way to solve problems [99]. Further, approximate solutions are of great use when handling noisy data [100]. As a result, the approximate solutions for the sparse systems which handle rank of the matrix provide a neat frame work for tomographic study on a quantum scale [101].

Shape sensitivity, parameterized domain, edge detection technique, elliptical boundary variational problems, adjoint method, mapping procedure, constraints on the domain, and gradient method aids in boundary studies along with numerical results are some of the vital applications of CTD [102, 113–115]. Study of elliptical boundary problems is important in finding the fundamental solutions, positive solutions and non-linear boundary value problem [116–122]. Treating mesh as equivalent to the

Table 2 Performance metrics of the denoising filters

Metrics	Mathematical Expression	Definition	Range
AD	$AD = \frac{1}{mn}\sum_{i=1}^{m}\sum_{j=1}^{n}\left[I_m(i,j) - I_m^F(i,j)\right]$	Mean difference between the original and the denoised image	AD is minimum for high quality denoised images and vice versa $AD = 0 \; to \; 255$
MSE	$MSE = \frac{1}{mn}\sum_{i=1}^{m}\sum_{j=1}^{n}\left(I_m(i,j) - I_m^F(i,j)\right)^2$	Average difference between the original and the denoised image	MSE is minimum for high quality denoised images and vice versa $MSE = 0 \; to \; 255$
RMSE	$RMSE = \sqrt{\frac{1}{mn}\sum_{i=1}^{m}\sum_{j=1}^{n}\left(I_m(i,j) - I_m^F(i,j)\right)^2}$	Square root of the difference between the square of noised image and the filtered image divided by the size of the original image	RMSE is minimum for high quality denoised images and vice versa
PSNR	$PSNR = 10\log_{10}\frac{(2^n-1)^2}{MSE} = 10\log_{10}\frac{255^2}{MSE}$	Quantitative measurement of distortion of the signal and a qualitative measurement for comparison of noise	PSNR is maximum for high quality denoised images and vice versa
MD	$MD = \max\left(\left\lvert I_m(i,j) - I_m^F(i,j)\right\rvert\right)$	Maximum error between the original image and filtered image	MD is minimum for high quality denoised images and vice versa
NAE	$NAE = \frac{\sum_{i=1}^{m}\sum_{j=1}^{n}\left\lvert\left[I_m(i,j)-I_m^F(i,j)\right]\right\rvert}{\sum_{i=1}^{m}\sum_{j=1}^{n}\left\lvert\left[I_m(i,j)\right]\right\rvert}$	Numerical variance of the filtered image w.r.t the original image	NAE is minimum for high quality denoised images and vice versa NAE = 0 ~ 1
NMSE	$NMSE = \frac{\sum_{i=1}^{m}\sum_{j=1}^{n}\left[I_m(i,j)-I_m^F(i,j)\right]^2}{\sum_{i=1}^{m}\sum_{j=1}^{n}\left[I_m(i,j)\right]^2}$	Measurement of the variation of MSE	NMSE is minimum for high quality denoised images and vice versa
SC	$SC = \frac{\sum_{i=1}^{m}\sum_{j=1}^{n}\left[I_m(i,j)\right]^2}{\sum_{i=1}^{m}\sum_{j=1}^{n}\left[I_m^F(i,j)\right]^2}$	Qualitative representation in terms of the correlation function and quantitative measurement for comparison of similarity between the original image and filtered image	$SC = 1 \Rightarrow I_m(i,j) = I_m^F(i,j)$
CC	$CC = \frac{\sum_{i=1}^{m}\sum_{j=1}^{n}\left[\left[I_m(i,j)-\bar{I}_m(i,j)\right]\left[I_m^F(i,j)-\bar{I}_m^F(i,j)\right]\right]}{\sqrt{\sum_{i=1}^{m}\sum_{j=1}^{n}\left[I_m(i,j)-\bar{I}_m(i,j)\right]^2}\sqrt{\sum_{i=1}^{m}\sum_{j=1}^{n}\left[I_m^F(i,j)-\bar{I}_m^F(i,j)\right]^2}}$	Inter-relationship between original and denoised image in terms of edge preservation	$CC = 0 \sim 1$ $CC = 1 \Rightarrow I_m(i,j) = I_m^F(i,j)$
NCC	$NCC = \frac{\sum_{i=1}^{m}\sum_{j=1}^{n} I_m(i,j)\cdot I_m^F(i,j)}{\sum_{i=1}^{m}\sum_{j=1}^{n}\left[I_m(i,j)\right]^2}$	Establishes degree of similarity between original and filtered images	$NCC = -1 \sim 1$
IQI	$IQI = \frac{4\sigma_{I_m I_m^F}\bar{I}_m\bar{I}_m^F}{\left(\sigma^2{}_{I_m}+\sigma^2{}_{I_m^F}\right)\left(\bar{I}_m^2+\bar{I}_m^{2F}\right)}$	Deformation in terms of loss of correlation, mean distortion and variance distortion	$IQI = -1 \sim 1$
SSIM	$SSIM = \frac{\left(2\bar{I}_m\bar{I}_m^F+c_1\right)\left(2\sigma_{I_m I_m^F}+c_2\right)}{\left(\bar{I}_m^2+\bar{I}_m^{2F}+c_1\right)\left(\sigma^2{}_{I_m}+\sigma^2{}_{I_m^F}+c_2\right)}$	Evaluates the degradation of the image and is considered as comparison metric for structure, contrast as well as luminance between the original image and the filtered image	$SSIM = 0 \sim 1$ $SSIM = 1 \Rightarrow I_m(i,j) = I_m^F(i,j)$
CNR	$CNR = \frac{\left\lvert\bar{I}_m-\bar{I}_m^F\right\rvert}{\sqrt{\sigma_{I_m}^2+\sigma_{I_m^F}^2}}$	Qualitative metric for identifying differences between two ROI	CNR is maximum for high quality denoised images and vice versa
NI	$NI = \frac{\sigma_{I_m^F}}{\bar{I}_m^F}$	An inherent property of imaging instrument and measurement of noise removal	NI is minimum for high quality denoised images and vice versa
ASNR	$ASNR = \frac{\bar{I}_m^F}{\sigma_{I_m^F}}$	Ratio of the mean value of the standard deviation and variation of noise to the mean value	ASNR is maximum for high quality denoised images and vice versa
IV	$IV = \frac{1}{mn}\sum_{i=1}^{m}\sum_{j=1}^{n}\left[I_m^F(i,j) - \bar{I}_m^F(i,j)\right]^2$	Quantitative metric for the description of factors present in noise and is independent of intensity	IV is minimum for high quality denoised images and vice versa
NSD	$NSD = \sqrt{\frac{1}{mn}\sum_{i=1}^{m}\sum_{j=1}^{n}\left[I_m^F(i,j) - I_m^{Fn}(i,j)\right]^2}$	Quantitative metric that describes noise reduction in images and narrates the constituents of noise present in the image	NSD is minimum for high quality denoised images and vice versa
ENL	$ENL = \frac{\left(I_m^{Fn}(i,j)\right)^2}{NSD^2}$	Quantitative metric for the estimation of noise present in images and a pivotal tool used for the statistical modelling of images	ENL is maximum for high quality denoised images and vice versa

arrangement of pixels in the medical image, one can evaluate the difference approximation for the elliptical boundary value problems [123]. Also, the elliptical boundary problem $\Psi[\Omega]$ is based on the solution of the state function Ψ, i.e., the shape functional. With this background the CTD can also be expressed as

$$\begin{aligned} D_T(\hat{x}) = {} & \mathit{Asymptotic\ analysis\ of\ solutions\ to\ elliptic\ Boundary\ value\ problems\ in\ singularlyperturbed\ domain} \\ & + \mathit{Asymptotic\ analysis\ of\ Shape\ functional}. \end{aligned}$$

The CTD was used to solve the denoising problems in CT and MR images and the algorithm for the same was tested for different images in the clinical examples as illustrated in the following sections.

Specification of tools

The proposed CTD and other tranditional denoising algorithms were tested in various CT and MR images, The image specification, hardware and the software details are given below. The CT and MR images in the Digital imaging and communication system (DICOM) format, which enables user-friendly interaction between Picture Archiving and Communication System (PACS) and Radiology Information Systems (RIS), were acquired from the scan facility available at Image Art, Vijaya Health Centre, Vadapalani, Chennai. The HRCT images were taken from SOMATOM dual-source CT, which is the fastest CT scan machine in the present scenario. All the HRCT scans were taken at 1.00 mm thick, 40 mm in beam length, and 400 mm in beam width (or Window Width). The images were acquired in 0° angle tilt or gantry tilt and 30.3 cm Display Field of View (DFOV). The operating power inputs of HRCT are 120 kV and 178 mA. The kernel used for soft tissue reconstruction is Br40f/3. The resolution of the images acquired is 480 × 340 (width x height) with a bit depth of 32 bits. Brain HRCT images are also collected from the same scan centre in spiral (SPI) mode. The brain MR images were acquired from the GE Healthcare SIGNA™ Explorer machine operating at 1.5 Tesla magnetic fields. We have collected and tested more than 300 HRCT and MR images for studying the denoising effect of the proposed algorithm. Of which, the results of five HRCT and MR images are given here for comparison. The algorithms were tested on an HP laptop with AMD Ryzen5 3500U processor, Radeon Vega mobile Gfx graphics card, 8 GB RAM, and MATLAB 2018a on a 64-bit Windows 10 system.

Clinical examples

The proposed CTD and traditional filters were tested on a HRCT image (Thoracic Cavity Carina, Head CT (Globe Lens 4th Ventricle), and nine MR images (six Middle Cerebral Artery territory of DWI, FLAIR T2, and PROP T2), and three neoplastic lesions (two PROP and FLAIR T1).

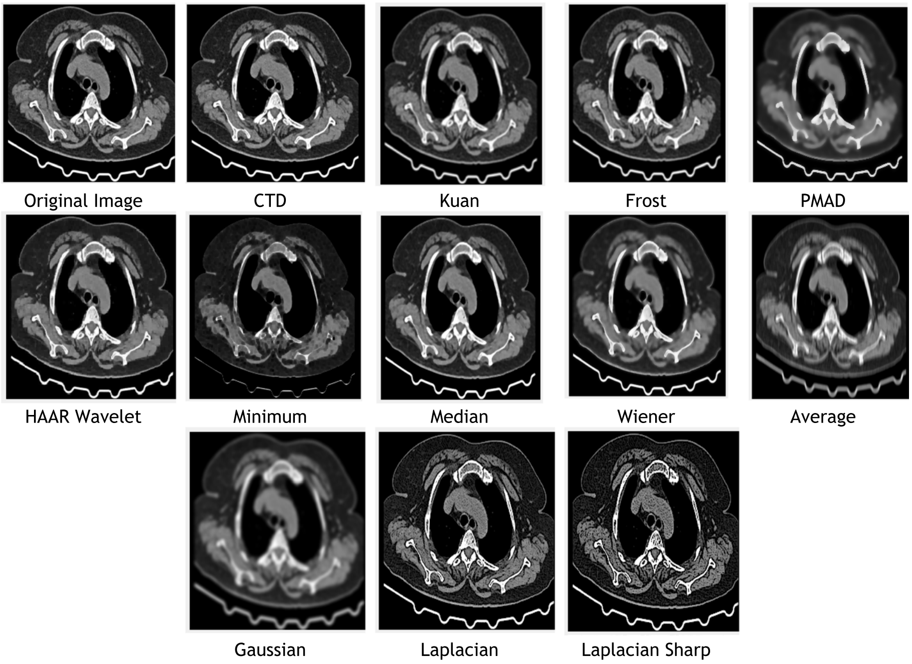
Original Image
CTD
Kuan
Frost
PMAD
HAAR Wavelet
Minimum
Median
Wiener
Average
Gaussian
Laplacian
Laplacian Sharp

Fig. 1 Original and denoised Images of Carina

Table 3 Quality metric for Carina

Metrics	Continuum TD	Kuan Filter	Frost Filter	PMAD Filter (15 itrs)	Wavelet	Ordinary Filter Min	Median Filter	Wiener Filter	Average Filter 7×7	Gaussian Filter	Laplacian Filter	Laplacian Filter Sharp
AD	0.0991	3.31	2.83	5.40	1.71	18.40	1.66	3.06	7.56	6.96	7.07	11.40
MSE	0.3853	26.61	23.07	44.10	14.11	95.88	13.66	30.75	40.56	41.75	51.81	65.84
RMSE	0.6207	5.15	4.80	6.64	3.75	9.79	3.69	5.54	6.36	6.46	7.19	8.11
PSNR	52.27	33.87	34.49	31.68	36.63	28.31	36.77	33.25	32.04	31.92	30.98	29.94
MD	34	116	111	97	21	255	181	72	205	154	180	220
NAE	0.0018	0.0628	0.0539	0.1026	3.26E-02	0.3494	0.0315	0.0581	0.1436	0.1322	0.1342	0.2165
NMSE	0.0024	0.1717	0.1492	0.2822	9.07E-02	0.6186	0.0885	0.1974	0.2607	0.2681	0.3360	0.4262
SC	1	0.9621	0.9695	0.9170	0.9903	1.08	0.9990	0.9534	0.9521	0.9005	1.17	1.39
CC	1	0.9816	0.9850	0.9667	0.9967	0.8535	0.9940	0.9883	0.8882	0.9268	0.9672	0.9274
NCC	1	1.0069	1.0067	1.0063	1.0017	0.9427	1.0005	1.0052	1.0042	1.0083	0.8850	0.7452
IQI	0.9986	0.9528	0.9560	0.8567	0.9364	0.7459	0.9851	0.8846	0.8906	0.8622	0.9646	0.9178
SSIM	0.9982	0.9041	0.9243	0.6925	0.9440	0.6465	0.9437	0.8353	0.7003	0.6655	0.8849	0.7985
CNR	1.50E-06	1.56E-04	8.05E-04	2.32E-04	2.97E-05	0.2311	0.0042	0.0037	0.0138	2.26E-04	0.0773	0.1246
NI	1.88E-05	1.75E-05	1.77E-05	1.69E-05	1.85E-05	2.05E-05	1.86E-05	1.77E-05	1.69E-05	1.57E-05	2.16E-05	2.38E-05
ASNR	5.32E+04	5.71E+04	5.64E+04	5.91E+04	5.42E+04	4.87E+04	5.37E+04	5.63E+04	5.90E+04	6.37E+04	4.64E+04	4.19E+04
IV	4.21E+03	3.65E+03	3.75E+03	3.40E+03	4.05E+03	2.12E+03	4.08E+03	3.80E+03	3.27E+03	2.93E+03	4.15E+03	4.15E+03
NSD	1.82E+08	1.82E+08	1.82E+08	1.82E+08	1.82E+08	7.69E+07	1.79E+08	1.84E+08	1.74E+08	1.82E+08	1.36E+08	1.12E+08
ENL	8.40E-14	8.40E-14	8.37E-14	8.40E-14	8.40E-14	1.98E-13	8.52E-14	8.29E-14	8.79E-14	8.40E-14	1.12E-13	1.37E-13

Table 4 Quality metric for globe lens 4th ventricle

Metrics	Continuum TD	Kuan Filter	Frost Filter	PMAD Filter(15 itrs)	Haar Wavelet	Ordinary Filter Min	Median Filter	Wiener Filter	Average Filter 7×7	Gaussian Filter	Laplacian Filter	Laplacian Filter Sharp
AD	9.00E-04	2.57	2.14	4.78	0.0095	17.002	0.9130	2.58	7.15	6.42	4.48	8.77
MSE	0.0035	22.09	18.30	43.75	0.0095	7.89E+01	7.005	26.11	41.96	43.76	32.03	43.07
RMSE	0.0598	4.70	4.27	6.61	0.0976	8.883875	2.64	5.10	6.47	6.61	5.66	6.56
PSNR	72.58	34.68	35.50	31.72	68.33	29.15	39.67	33.96	31.90	31.71	33.07	31.78
MD	11	130	124	136	1	255	163	74	192	176	168	209
NAE	1.24E-05	0.0353	0.0294	0.0657	1.31E-04	0.2334	0.0125	0.0354	0.0982	0.0881	0.0615	0.1204
NMSE	3.13E-05	0.1629	0.1348	0.3270	6.78E-05	0.5939	0.0502	0.1940	0.3162	0.3271	0.2479	0.3377
SC	1	0.9431	0.9525	0.8708	1	1.15	1	0.9193	0.9297	0.8718	1.06	1.14
CC	1	1	1	0.9856	1	0.9187	1	1	0.9545	0.9655	1	0.9627
NCC	1	1.0126	1.0119	1.0137	1	0.8954	1	1.01	1.006	1.01	0.9438	0.8858
IQI	1	0.9816	0.9534	0.8939	1	0.7445	0.9705	0.9146	1.011	0.9263	0.9705	0.9500
SSIM	1	0.9485	0.9611	0.7866	1	0.7096	0.9760	0.9005	0.7800	0.7667	0.9405	0.8516
CNR	3.65E-07	1.74E-05	4.98E-04	1.20E-04	1.97E-05	0.1443	6.76E-04	2.56E-04	0.0137	3.97E-05	0.0358	0.0700
NI	1.86E-05	1.80E-05	1.81E-05	1.75E-05	1.86E-05	2.11E-05	1.86E-05	1.80E-05	1.78E-05	1.69E-05	1.97E-05	2.10E-05
ASNR	5.38E+04	5.57E+04	5.54E+04	5.70E+04	5.38E+04	4.73E+04	5.38E+04	5.55E+04	5.63E+04	5.92E+04	5.07E+04	4.75E+04
IV	7.88E+03	7.35E+03	7.45E+03	7.01E+03	7.88E+03	5.98E+03	7.85E+03	7.40E+03	6.86E+03	6.50E+03	7.80E+03	7.80E+03
NSD	3.48E+08	3.48E+08	3.48E+08	3.48E+08	3.48E+08	2.04E+08	3.47E+08	3.48E+08	3.32E+08	3.48E+08	3.06E+08	2.69E+08
ENL	4.39E-14	4.39E-14	4.38E-14	4.39E-14	4.39E-14	7.47E-14	4.40E-14	4.39E-14	4.60E-14	4.39E-14	4.98E-14	5.67E-14

Table 5 Quality metric for MCA DWI (B 800) MRI

Metrics	Continuum TD	Kuan Filter	Frost Filter	PMAD Filter(15 itrs)	Haar Wavelet	Ordinary Filter Min	Median Filter	Wiener Filter	Average Filter 7×7	Gaussian Filter	Laplacian Filter	Laplacian Filter Sharp
AD	1.10E-01	0.8712	0.6221	3.43	1.40	9.56	0.4974	1.48	4.06	2.63	2.55	6.16
MSE	0.1417	3.25	1.83	33.11	7.39	8.33E+01	1.74	9.00	33.20	24.00	21.71	52.10
RMSE	3.77E-01	1.80	1.35	5.75	2.71	9.12	1.32	3.00	5.76	4.90	4.66	7.21
PSNR	56.61	43.00	45.50	32.93	39.44	28.92	45.71	38.58	32.91	34.32	34.76	30.96
MD	6	17	14	49	16	88	19	25	86	43	74	125
NAE	1.38E-03	0.0109	0.0078	0.0431	1.76E-02	0.1201	0.0062	0.0186	0.0509	0.0331	0.0320	0.0773
NMSE	6.36E-04	0.0182	0.0102	0.1884	4.13E-02	0.4745	0.0097	0.0509	0.1942	0.1354	0.1232	0.2995
SC	1	1	1	0.9796	1	1.08	1	1	1.02	0.9846	1.04	1.08
CC	1	1	1	0.9895	1	0.9876	1	1	0.9883	1	1	0.9859
NCC	1	1	1	1.0094	1	0.9553	1	1	0.9888	1.006	0.9719	0.9316
IQI	0.9837	0.9652	0.9820	0.8440	0.9071	0.8886	0.9677	0.9063	0.8497	0.8627	0.9675	0.9211
SSIM	1	0.9808	0.9882	0.8012	0.9429	0.8641	0.9865	0.9305	0.8513	0.8774	0.9557	0.8396
CNR	2.30E-05	8.24E-05	1.19E-03	6.86E-04	1.43E-04	0.0991	9.49E-05	4.77E-04	0.0185	2.73E-05	0.0256	0.0621
NI	1.35E-05	1.34E-05	1.34E-05	1.29E-05	1.34E-05	1.44E-05	1.34E-05	1.33E-05	1.36E-05	1.31E-05	1.39E-05	1.46E-05
ASNR	7.42E+04	7.48E+04	7.48E+04	7.73E+04	7.46E+04	6.95E+04	7.44E+04	7.51E+04	7.35E+04	7.66E+04	7.18E+04	6.87E+04
IV	4.95E+03	4.86E+03	4.88E+03	4.55E+03	4.90E+03	4.36E+03	4.92E+03	4.82E+03	4.81E+03	4.64E+03	4.96E+03	4.92E+03
NSD	4.16E+08	4.16E+08	4.17E+08	4.15E+08	4.16E+08	3.22E+08	4.16E+08	4.15E+08	3.97E+08	4.16E+08	3.90E+08	3.54E+08
ENL	3.67E-14	3.67E-14	3.66E-14	3.68E-14	3.67E-14	4.74E-14	3.67E-14	3.67E-14	3.84E-14	3.67E-14	3.92E-14	4.31E-14

Table 6 Quality metric for MCA FLAIR T2

Metrics	Continuum TD	Kuan Filter	Frost Filter	PMAD Filter (15 itrs)	Haar Wavelet	Ordinary Filter Min	Median Filter	Wiener Filter	Average Filter 7×7	Gaussian Filter	Laplacian Filter	Laplacian Filter Sharp
AD	9.16E-02	1.44	1.09	4.42	1.35	11.89	0.7067	1.79	4.89	3.98	3.43	6.82
MSE	0.1395	10.98	7.30	36.46	7.53	8.12E+01	4.34	14.68	35.23	31.87	31.64	55.42
RMSE	3.74E-01	3.31	2.70	6.03	2.74	9.009	2.08	3.83	5.93	5.64	5.62	7.44
PSNR	56.68	37.72	39.49	32.51	39.36	29.03	41.75	36.46	32.66	33.09	33.12	30.69
MD	8	45	35	92	16	144	54	33	117	87	86	167
NAE	1.46E-03	0.0229	0.0174	0.0704	2.15E-02	0.1891	0.0112	0.0285	0.0777	0.0633	0.0545	0.1085
NMSE	6.58E-04	0.0557	0.0373	0.1987	4.05E-02	0.4380	0.0218	0.0811	0.1987	0.1693	0.1712	0.3114
SC	1	0.9816	0.9837	0.9534	1	1.07	1	0.9752	1	0.9629	1.07	1.15
CC	1	1	1	0.9587	1	0.9354	1	1	0.9406	0.9629	1	0.9662
NCC	1	1	1	1.02	1.002	0.9667	1.002	1.01	1.003	1.021	0.9408	0.8806
IQI	0.9547	0.9205	0.9276	1.11	0.8621	0.6844	0.9293	0.8569	0.8298	0.8931	0.9754	0.9485
SSIM	1	0.9693	0.9796	0.7504	0.9532	0.7988	0.9824	0.9162	0.8089	0.8151	0.9460	0.8299
CNR	1.15E-04	1.20E-04	1.60E-03	4.16E-04	8.22E-05	0.1740	1.54E-03	8.72E-04	0.0206	1.45E-04	0.0472	0.0937
NI	1.23E-05	1.19E-05	1.20E-05	1.10E-05	1.22E-05	1.37E-05	1.22E-05	1.19E-05	1.20E-05	1.11E-05	1.33E-05	1.42E-05
ASNR	8.10E+04	8.40E+04	8.35E+04	9.09E+04	8.22E+04	7.33E+04	8.19E+04	8.43E+04	8.36E+04	9.04E+04	7.53E+04	7.05E+04
IV	2.59E+03	2.41E+03	2.45E+03	2.06E+03	2.52E+03	2.08E+03	2.52E+03	2.40E+03	2.32E+03	2.08E+03	2.68E+03	2.72E+03
NSD	2.59E+08	2.59E+08	2.60E+08	2.59E+08	2.59E+08	1.71E+08	2.59E+08	2.60E+08	2.48E+08	2.59E+08	2.32E+08	2.06E+08
ENL	5.88E-14	5.88E-14	5.86E-14	5.89E-14	5.88E-14	8.94E-14	5.90E-14	5.87E-14	6.16E-14	5.88E-14	6.58E-14	7.40E-14

Table 7 Quality metric for MCA PROP T2

Metrics	Continuum TD	Kuan Filter	Frost Filter	PMAD Filter (15 itrs)	Haar Wavelet	Ordinary Filter Min	Median Filter	Wiener Filter	Average Filter 7 × 7	Gaussian Filter	Laplacian Filter (Lap,0,replicate)	Laplacian Filter Sharp (1 1 1; 1 -8 1; 1 1 1)
AD	1.16E-01	1.70	1.36	4.21	1.34	3.76	1.02	1.74	4.68	3.76	4.68	10.22
MSE	0.2539	14.11	10.90	35.23	7.68	3.01E + 01	7.66	13.92	34.28	30.08	39.05	63.84
RMSE	5.04E-01	3.75	3.30	5.93	2.77	5.48	2.76	3.73	5.85	5.48	6.24	7.99
PSNR	54.08	36.63	37.75	32.66	39.27	33.34	39.28	36.69	32.78	33.34	32.21	30.07
MD	24	51	44	82	16	97	56	41	127	97	122	163
NAE	1.71E-03	0.0251	0.020	0.0619	1.97E-02	0.0553	0.0151	0.0255	0.0687	0.0553	0.0687	0.1501
NMSE	1.23E-03	0.0812	0.0625	0.2060	4.41E-02	0.1759	0.0433	0.0788	0.2061	0.1759	0.2282	0.3769
SC	1	0.98	0.9868	0.9634	1	0.9703	1	0.9776	1	0.9703	1.06	1.13
CC	1	1	1	0.9807	1	0.9811	1	1	0.9762	0.9811	0.9885	0.9494
NCC	1	1.006	1.006	1.014	1.00	1.01	1	1	1.001	1.01	0.9543	0.8963
IQI	0.9384	0.8961	0.9128	0.7689	0.8288	0.8151	0.9126	0.8220	0.7995	0.8151	0.9530	0.9242
SSIM	1	0.9528	0.9665	0.7629	0.9546	0.8125	0.9728	0.9142	0.8083	0.8125	0.9152	0.7683
CNR	1.64E-05	1.11E-04	1.28E-03	5.46E-04	3.80E-04	3.78E-05	2.94E-03	1.62E-03	0.0165	3.78E-05	0.0490	0.1073
NI	1.52E-05	1.49E-05	1.49E-05	1.44E-05	1.51E-05	1.44E-05	1.51E-05	1.49E-05	1.50E-05	1.44E-05	1.62E-05	1.76E-05
ASNR	6.58E + 04	6.70E + 04	6.69E + 04	6.94E + 04	6.63E + 04	6.92E + 04	6.62E + 04	6.69E + 04	6.65E + 04	6.92E + 04	6.18E + 04	5.67E + 04
IV	4.61E + 03	4.43E + 03	1.49E-05	4.13E + 03	4.54E + 03	4.16E + 03	4.51E + 03	4.47E + 03	4.30E + 03	4.16E + 03	4.52E + 03	4.48E + 03
NSD	3.04E + 08	3.04E + 08	3.05E + 08	3.04E + 08	3.04E + 08	3.04E + 08	3.01E + 08	3.05E + 08	2.90E + 08	3.04E + 08	2.64E + 08	2.20E + 08
ENL	5.02E-14	5.02E-14	5.00E-14	5.03E-14	5.01E-14	5.02E-14	5.06E-14	5.00E-14	5.26E-14	5.02E-14	5.79E-14	6.95E-14

Table 8 Quality metric for acute infarct

Metrics	Continuum TD	Kuan Filter	Frost Filter	PMAD Filter (15 itrs)	Wavelet	Ordinary Filter Min	Median Filter	Wiener Filter	Average Filter 7×7	Gaussian Filter	Laplacian Filter	Laplacian Filter Sharp
AD	0.0214	0.5456	0.2986	1.95	0.5211	5.60	0.2165	0.7652	2.67	1.41	1.33	3.29
MSE	0.0228	1.65	0.6689	16.61	1.12	43.44	0.4633	2.86	18.87	10.02	8.76	30.58
RMSE	0.1512	1.28	0.8179	4.07	1.06	6.59	0.6806	1.69	4.34	3.16	2.96	5.53
PSNR	64.54	45.94	49.87	35.92	47.60	31.75	51.47	43.56	35.37	38.12	38.70	33.27
MD	3	107	14	37	6	107	9	14	92	48	45	82
NAE	2.95E-04	0.0075	0.0041	0.0269	0.0072	0.0771	0.0030	0.0105	0.0368	0.0195	0.0183	0.0453
NMSE	1.12E-04	0.0103	0.0040	0.1050	0.0069	0.2775	0.0028	0.0181	0.1242	0.0614	0.0538	0.1980
SC	1	1	0.9965	0.9845	1	1.06	1	0.9975	1.01	0.9906	1.02	1.05
CC	1	1	1	0.9972	1	0.9933	1	1	0.9941	0.9980	1	0.9960
NCC	1	0.9973	1	1	1	0.9635	1	1	0.9912	1	0.9842	0.9581
IQI	0.9891	0.9667	0.9773	0.8180	0.9213	0.8731	0.9726	0.9289	0.8767	0.9113	0.9823	0.9121
SSIM	1	0.9868	0.9938	0.8896	0.9835	0.9159	0.9941	0.9672	0.9264	0.9378	0.9738	0.8898
CNR	2.13E-05	0.0011	8.67E-04	8.90E-04	7.45E-05	0.0518	1.32E-04	1.74E-04	0.0153	1.05E-04	0.0121	0.0301
NI	1.64E-05	1.64E-05	1.64E-05	1.61E-05	1.64E-05	1.72E-05	1.64E-05	1.64E-05	1.66E-05	1.62E-05	1.67E-05	1.70E-05
ASNR	6.08E+04	6.09E+04	6.10E+04	6.19E+04	6.10E+04	5.80E+04	6.09E+04	6.10E+04	6.00E+04	6.17E+04	5.98E+04	5.85E+04
IV	6.02E+03	5.98E+03	5.99E+03	5.80E+03	6.01E+03	5.62E+03	6.01E+03	5.97E+03	5.92E+03	5.85E+03	5.99E+03	5.92E+03
NSD	3.43E+08	3.42E+08	3.43E+08	3.42E+08	3.42E+08	2.92E+08	3.42E+08	3.42E+08	3.27E+08	3.42E+08	3.30E+08	3.12E+08
ENL	4.48E-14	4.50E-14	4.47E-14	4.45E-14	4.48E-14	5.26E-14	4.48E-14	4.48E-14	4.70E-14	4.48E-14	4.65E-14	4.92E-14

Table 9 Quality metrics of ischemic demyelination disease

Metrics	Continuum TD	Kuan Filter	Frost Filter	PMAD Filter (15 itrs)	Wavelet	Ordinary Filter Min	Median Filter	Wiener Filter	Average Filter 7×7	Gaussian Filter	Laplacian Filter	Laplacian Filter Sharp
AD	0.0353	0.7771	0.4725	2.25	0.8091	5.90	0.4055	0.9487	2.29	1.75	1.91	4.43
MSE	0.0437	3.18	1.64	20.57	2.99	47.85	1.41	4.82	16.07	14.41	15.66	37.11
RMSE	0.2091	1.78	1.28	4.53	1.72	6.91	1.18	2.19	4.01	3.79	3.95	6.09
PSNR	61.72	43.10	45.96	34.99	43.37	31.33	46.62	41.29	36.06	36.54	36.18	32.43
MD	5	138	16	57	11	138	26	19	118	58	64	101
NAE	6.91E-04	0.0152	0.0092	0.0441	0.0158	0.1156	0.0079	0.0185	0.0449	0.0343	0.0374	0.0867
NMSE	2.31E-04	0.0238	0.0122	0.1591	0.0223	0.3724	0.0106	0.0360	0.1288	0.1101	0.1213	0.2936
SC	1	0.9939	0.9887	0.9599	0.9948	1.12	0.9992	0.9821	1	0.9668	1.05	1.09
CC	1	0.9974	0.9995	0.9921	1	0.9885	1	0.9988	0.9915	0.9943	0.9977	0.9868
NCC	1	1	1	1.01	1	0.9388	0.9993	1	0.9923	1.01	0.9657	0.9261
IQI	.99	0.9397	0.9493	0.9737	0.9095	0.6706	0.9380	0.8278	0.8357	0.8664	0.9450	0.8979
SSIM	1	0.9766	0.9873	0.8457	0.9640	0.8839	0.9869	0.9443	0.9131	0.8973	0.9557	0.8546
CNR	2.46E-05	0.0016	0.0012	0.0010	2.68E-04	0.0710	4.81E-04	2.18E-05	0.0138	8.6E-05	0.0222	0.0521
NI	1.83E-05	1.83E-05	1.82E-05	1.78E-05	1.82E-05	1.92E-05	1.83E-05	1.82E-05	1.85E-05	1.79E-05	1.88E-05	1.95E-05
ASNR	5.45E+04	5.47E+04	5.48E+04	5.59E+04	5.46E+04	5.18E+04	5.46E+04	5.48E+04	5.39E+04	5.56E+04	5.30E+04	5.12E+04
IV	3.72E+03	3.67E+03	3.68E+03	3.51E+03	3.69E+03	3.21E+03	3.69E+03	3.67E+03	3.62E+03	3.56E+03	3.64E+03	3.50E+03
NSD	1.69E+08	1.69E+08	1.70E+08	1.69E+08	1.70E+08	1.32E+08	1.69E+08	1.69E+08	1.62E+08	1.69E+08	1.57E+08	1.42E+08
ENL	9.05E-14	9.10E-14	9.01E-14	9.08E-14	9.04E-14	1.15E-13	9.06E-14	9.05E-14	9.48E-14	9.05E-14	9.76E-14	1.09E-13

Table 10 Quality metrics of cerebral infarct

Metrics	Continuum TD	Kuan Filter	Frost Filter	PMAD Filter (15 itrs)	Wavelet	Ordinary Filter Min	Median Filter	Wiener Filter	Average Filter 7×7	Gaussian Filter	Laplacian Filter	Laplacian Filter Sharp
AD	0.0134	0.3700	0.2385	1.81	0.4802	4.52	0.1733	0.6146	2.10	1.21	1.22	2.97
MSE	0.0137	0.8863	0.4715	14.71	0.9813	36.69	0.3560	1.89	15.07	8.07	6.81	26.14
RMSE	0.1171	0.9414	0.6867	3.83	0.9906	6.05	0.5967	1.37	3.88	2.84	2.61	5.11
PSNR	66.75	48.65	51.39	36.45	48.21	32.48	52.61	45.35	36.35	39.05	39.79	33.95
MD	3	15	12	44	6	79	12	14	90	37	57	87
NAE	2.68E-04	0.0074	0.0048	0.0361	0.0096	0.0904	0.0035	0.0123	0.0420	0.0241	0.0244	0.0595
NMSE	6.04E-05	0.0053	0.0028	0.0913	0.0061	0.2283	0.0021	0.0120	0.0981	0.0486	0.0410	0.1674
SC	1	0.9959	0.9942	0.9689	1	1.04	1	0.9921	1.01	0.9818	1.02	1.06
CC	1	0.9997	0.9998	0.9941	0.9997	0.9925	1	0.9993	0.9924	0.9969	0.9989	0.9934
NCC	1	1	1	1.01	0.9997	0.9754	0.9997	1	0.9915	1	0.9850	0.9567
IQI	0.9805	0.9390	0.9355	0.7695	0.8484	0.8259	0.9490	0.8457	0.8403	0.8396	0.9133	0.8523
SSIM	1	0.9912	0.9947	0.8979	0.9847	0.9353	0.9957	0.9759	0.9299	0.9485	0.9742	0.8962
CNR	1.84E-06	1.35E-04	0.0015	7.06E-04	2.37E-04	0.0620	1.10E-04	3.72E-05	0.0155	5.81E-05	0.0163	0.0399
NI	1.63E-05	1.62E-05	1.62E-05	1.58E-05	1.63E-05	1.69E-05	1.63E-05	1.62E-05	1.65E-05	1.60E-05	1.66E-05	1.71E-05
ASNR	6.13E+04	6.15E+04	6.16E+04	6.30E+04	6.14E+04	5.90E+04	6.14E+04	6.16E+04	6.05E+04	6.25E+04	6.00E+04	5.84E+04
IV	2.82E+03	2.79E+03	2.80E+03	2.66E+03	2.81E+03	2.51E+03	2.81E+03	2.78E+03	2.75E+03	2.71E+03	2.80E+03	2.75E+03
NSD	1.63E+08	1.63E+08	1.63E+08	1.63E+08	1.63E+08	1.34E+08	1.63E+08	1.63E+08	1.55E+08	1.63E+08	1.55E+08	1.44E+08
ENL	9.44E-14	9.44E-14	9.39E-14	9.45E-14	9.43E-14	1.14E-13	9.44E-14	9.43E-14	9.89E-14	9.44E-14	9.91E-14	1.07E-13

Table 11 Quality metrics of neoplastic lesion 1 glioma

Metrics	Continuum TD	Kuan Filter	Frost Filter	PMAD Filter(15 itrs)	Haar Wavelet	Ordinary Filter Min	Median Filter	Wiener Filter	Average Filter 7×7	Gaussian Filter	Laplacian Filter	Laplacian Filter Sharp
AD	0.1539	1.71	1.42	4.06	1.37	10.67	1.19	1.65	4.39	3.52	4.49	8.69
MSE	0.3562	14.01	11.27	32.37	8.04	75.72	9.09	13.20	33.17	27.92	38.51	63.25
RMSE	0.5968	3.74	3.35	5.69	2.83	8.70	3.01	3.63	5.76	5.28	6.20	7.95
PSNR	52.61	36.66	37.61	33.03	39.07	29.33	38.54	36.92	32.92	33.67	32.27	30.12
MD	23	53	45	104	16	154	57	38	101	97	101	175
NAE	0.0032	0.0360	0.0298	0.0855	0.0288	0.2246	0.0250	0.0348	0.0924	0.0742	0.0945	0.1828
NMSE	0.0017	0.0764	0.0612	0.1816	0.0452	0.4241	0.0506	0.0762	0.1931	0.1550	0.2216	0.3710
SC	1	0.9794	0.9814	0.9177	0.9913	1.11	0.9957	0.9693	0.9839	0.9370	1.07	1.17
CC	1	0.9914	0.9936	0.9592	0.9964	0.9332	0.9955	0.9936	0.9444	0.9640	0.9770	0.9342
NCC	1	1	1	1.02	1	0.9416	1	1	1	1.02	0.9469	0.8718
IQI	0.9557	0.9246	0.9150	0.9204	0.8644	0.6707	0.9365	0.8660	0.8622	0.8589	0.9456	0.9352
SSIM	1	0.9411	0.9564	0.7368	0.9480	0.7241	0.9634	0.9084	0.7876	0.7993	0.8918	0.7414
CNR	2.15E-06	1.52E-04	0.0018	0.0010	5.31E-04	0.1783	0.0071	0.0030	0.0175	7.15E-05	0.0698	0.1348
NI	1.47E-05	1.42E-05	1.42E-05	1.31E-05	1.45E-05	1.62E-05	1.45E-05	1.42E-05	1.42E-05	1.33E-05	1.62E-05	1.80E-05
ASNR	6.78E+04	7.03E+04	7.00E+04	7.60E+04	6.88E+04	6.17E+04	6.86E+04	7.03E+04	7.04E+04	7.50E+04	6.15E+04	5.53E+04
IV	2.07E+03	1.93E+03	1.95E+03	1.64E+03	2.01E+03	1.51E+03	1.98E+03	1.94E+03	1.84E+03	1.69E+03	2.07E+03	2.08E+03
NSD	1.47E+08	1.47E+08	1.47E+08	1.47E+08	1.47E+08	8.83E+07	1.44E+08	1.48E+08	1.40E+08	1.47E+08	1.20E+08	9.81E+07
ENL	1.04E-13	1.04E-13	1.04E-13	1.04E-13	1.04E-13	1.74E-13	1.06E-13	1.03E-13	1.09E-13	1.04E-13	1.27E-13	1.56E-13

Table 12 Quality Metrics for neoplastic lesion 2—4th ventricle tumour

Metrics	Continuum TD	Kuan Filter	Frost Filter	PMAD Filter(15 itrs)	Haar Wavelet	Ordinary Filter Min	Median Filter	Wiener Filter	Average Filter 7×7	Gaussian Filter	Laplacian Filter	Laplacian Filter Sharp
AD	0.1211	1.69	1.37	4.14	1.37	10.77	1.11	1.67	4.11	3.59	4.39	9.12
MSE	0.2573	13.60	10.75	32.61	8.16	74.80	8.42	13.42	30.89	28.06	36.91	62.32
RMSE	0.5072	3.68	3.27	5.71	2.85	8.64	2.90	3.66	5.55	5.30	6.07	7.89
PSNR	54.03	36.79	37.81	32.99	39.01	29.39	38.87	36.85	33.23	33.65	32.46	30.18
MD	14	57	52	88	16	183	81	35	123	109	110	159
NAE	0.0023	0.0328	0.0264	0.0799	0.0264	0.2079	0.0213	0.0322	0.0794	0.0693	0.0847	0.1760
NMSE	0.0013	0.0716	0.0562	0.1798	0.0456	0.4178	0.0456	0.07780	0.1769	0.1519	0.2094	0.3619
SC	1	0.9773	0.9802	0.9323	0.9911	1.09	0.9950	0.9733	0.9862	0.9429	1.05	1.14
CC	1	0.9916	0.9940	0.9583	0.9966	0.9301	0.9961	0.9939	0.9567	0.9618	0.9798	0.9256
NCC	1	1	1	1.02	1	0.9459	1	1	1	1.02	0.9606	0.8931
IQI	0.9396	0.8977	0.9120	0.7645	0.8399	0.7145	0.9128	0.8243	0.8212	0.8086	0.9242	0.8703
SSIM	1	0.9471	0.9628	0.7397	0.9496	0.7405	0.9704	0.9097	0.8095	0.8013	0.9002	0.7386
CNR	1.81E-05	2.83E-04	0.0019	0.0012	2.99E-04	0.1757	0.0062	0.0026	0.0185	3.48E-05	0.0665	0.1379
NI	1.39E-05	1.34E-05	1.34E-05	1.27E-05	1.36E-05	1.48E-05	1.37E-05	1.34E-05	1.34E-05	1.26E-05	1.50E-05	1.68E-05
ASNR	7.19E+04	7.47E+04	7.44E+04	8.02E+04	7.31E+04	6.73E+04	7.30E+04	7.43E+04	7.41E+04	7.93E+04	6.63E+04	5.94E+04
IV	2.19E+03	2.03E+03	2.06E+03	1.76E+03	2.12E+03	1.57E+03	2.09E+03	2.06E+03	1.97E+03	1.80E+03	2.15E+03	2.18E+03
NSD	1.74E+08	1.74E+08	1.75E+08	1.74E+08	1.75E+08	1.09E+08	1.72E+08	1.75E+08	1.67E+08	1.75E+08	1.46E+08	1.18E+08
ENL	8.80E-14	8.81E-14	8.76E-14	8.82E-14	8.80E-14	1.40E-13	8.94E-14	8.75E-14	9.22E-14	8.80E-14	1.05E-13	1.29E-13

Table 13 Quality metrics for neoplastic lesion Ax T1 FLAIR glioma

Metrics	Continuum TD	Kuan Filter	Frost Filter	PMAD Filter(15 itrs)	Haar Wavelet	Ordinary Filter Min	Median Filter	Wiener Filter	Average Filter 7×7	Gaussian Filter	Laplacian Filter	Laplacian Filter Sharp
AD	0.0907	1.01	0.7424	3.24	0.9452	7.62	0.5592	1.20	3.59	2.36	3.03	6.76
MSE	0.1522	5.48	3.58	28.48	3.48	63.03	2.71	6.01	26.69	20.25	26.32	55.34
RMSE	0.3902	2.34	1.89	5.33	1.87	7.93	1.64	2.45	5.16	4.50	5.13	7.43
PSNR	56.30	40.73	42.58	33.58	42.70	30.13	43.80	40.34	33.86	35.06	33.92	30.70
MD	12	56	45	109	11	114	70	22	115	106	67	118
NAE	0.0014	0.0156	0.0115	0.0501	0.0146	0.1178	0.0086	0.0186	0.0555	0.0365	0.0467	0.1045
NMSE	7.55E-04	0.0298	0.0196	0.1462	0.0185	0.3283	0.0147	0.0309	0.1482	0.1045	0.1385	0.2937
SC	1	0.9921	0.9906	0.9622	0.9955	1.05	1	0.9870	1	0.9715	1.05	1.12
CC	1	0.9974	0.9984	0.9788	0.9985	0.9758	0.9987	0.9974	0.9726	0.9865	0.9927	0.9676
NCC	1	1	1	1.02	1	0.9762	1	1	0.9988	1.01	0.9629	0.9046
IQI	0.9410	0.9235	0.9109	0.7746	0.8514	0.0828	0.9198	0.7457	0.8106	0.8740	0.9093	0.5315
SSIM	0.9977	0.9694	0.9809	0.8012	0.9675	0.8551	0.9821	0.9459	0.8413	0.8732	0.9309	0.7741
CNR	1.24E-05	3.10E-04	0.0018	0.0022	2.52E-04	0.1142	8.96E-04	1.11E-04	0.0221	2.76E-06	0.0441	0.0979
NI	1.14E-05	1.13E-05	1.13E-05	1.08E-05	1.13E-05	1.24E-05	1.14E-05	1.13E-05	1.15E-05	1.10E-05	1.21E-05	1.31E-05
ASNR	8.73E+04	8.84E+04	8.84E+04	9.18E+04	8.78E+04	8.05E+04	8.76E+04	8.85E+04	8.69E+04	9.09E+04	8.21E+04	7.62E+04
IV	2.33E+03	2.26E+03	2.27E+03	2.09E+03	2.30E+03	2.12E+03	2.30E+03	2.26E+03	2.24E+03	2.14E+03	2.39E+03	2.44E+03
NSD	2.72E+08	2.72E+08	2.73E+08	2.71E+08	2.72E+08	2.12E+08	2.72E+08	2.72E+08	2.60E+08	2.72E+08	2.47E+08	2.18E+08
ENL	5.64E-14	5.64E-14	5.62E-14	5.67E-14	5.64E-14	7.25E-14	5.65E-14	5.64E-14	5.91E-14	5.64E-14	6.21E-14	7.03E-14

AD

MSE

RMSE

PSNR

MD

NAE

NMSE

SC

CC

NCC

IQI

SSIM

Reciprocal CNR

NI

ASNR

IV

NSD

ENL

Fig. 2 Histogram plots of the quality metrics of Carina

Quality metrics were computed using denoised and original images to compare the efficiency of filters in handling quantum mottle and Gaussian/Rayleigh noises in CT and MR images respectively. A radiographic expert assessed image quality through visual inspection. Clinical example images, estimated quality metrics, and histogram plots are presented in Figs. 1, 3, 5, 7, 9, 11, 13, 15, 17, 19, 21, Tables 3, 4, 5, 6, 7, 8, 9, 10, 11, 12 and 13, and histogram plots in Figs. 2, 4, 6, 8, 10, 12, 14, 16, 18, 20, 22 respectively.

Clinical example 1: HRCT thoracic cavity carina

The study focuses on the role of Carina in chest CT imaging for detecting tracheobronchial carcinoid tumors [124]. Quantum mottle noise in CT images often obscures the carina morphology due to vascular matter in the lungs. The proposed denoising technique (CTD) effectively addresses this issue, producing clear and high-resolution images. Inferences from HRCT carina filtered images, metrics, and histogram plots (Fig. 1, Table 3 and Fig. 2) are summarized as follows:

a) CTD exhibited significantly lower values in AD, MSE, RMSE, MD, NAE, and NMSE compared to traditional filters, showcasing exceptional denoising capability, particularly in reducing quantum mottle noise. Radiographers noted the CTD denoised image's ability to delineate the carina point with complete opacity on both sides, aiding surgeons and anesthesiologists in accurate findings for post-pneumonectomy-like syndrome severity.

b) SC, CC, NCC, IQI, and SSIM returned unity values for CTD, retaining all structural information in carina HRCT, unlike other filters. The cartilaginous ridge shape of the carina and the surrounding lungs cavity were exceptionally retained in the denoised CTD image.

c) PSNR recorded a 30% higher value for CTD, attesting to its ability to produce a high-quality, quantum mottle-free carina image. CNR, NI, ASNR, IV, NSD, and ENL scores were notable for CTD, highlighting its fine contrast, noise-free, and radiologically preserved carina image.

d) Ultimately, the CTD denoised image accurately retained radiological features of the carina while eliminating quantum mottle noise, as confirmed by visual inspection from a radiological expert.

Clinical example 2: Ocular globe-lens 4th ventricle head CT

The cerebral ventricular system, a protective unit filled with cerebrospinal fluid, indicates brain health. Deformities in this system signal potential brain diseases [125]. The system comprises four ventricles, with the fourth ventricle located between the cerebellum and pons/medulla. In CT imaging, an irregularly shaped fourth ventricle may indicate meningioma tumours [126, 127]. The ocular globe's structure is crucial in cases like orbital trauma and retinoblastoma [128, 129]. A CTD denoised image impressed a radiographer, showcasing

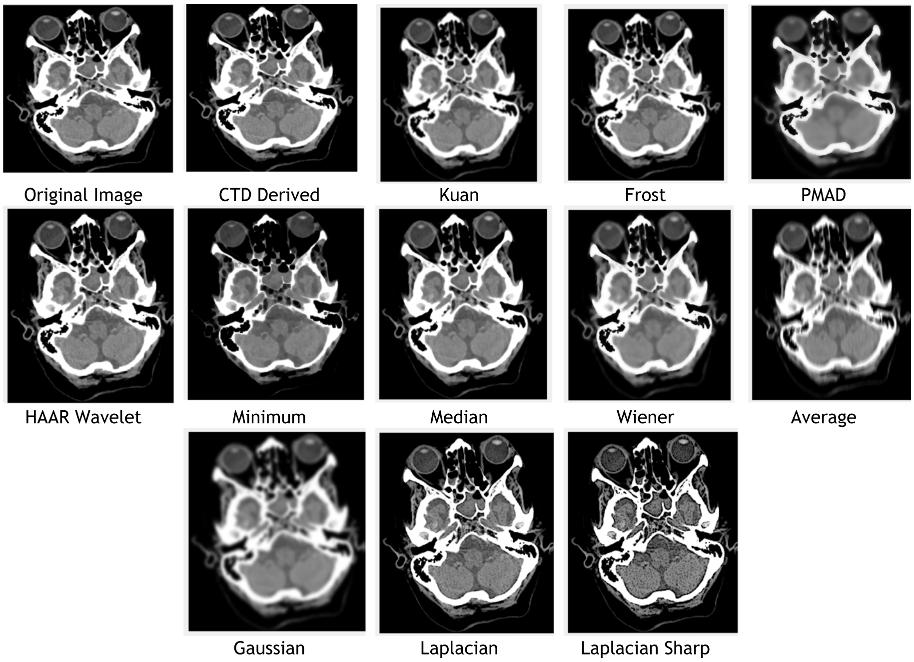

Fig. 3 Original and denoised Images of Globe Lens 4th Ventricle

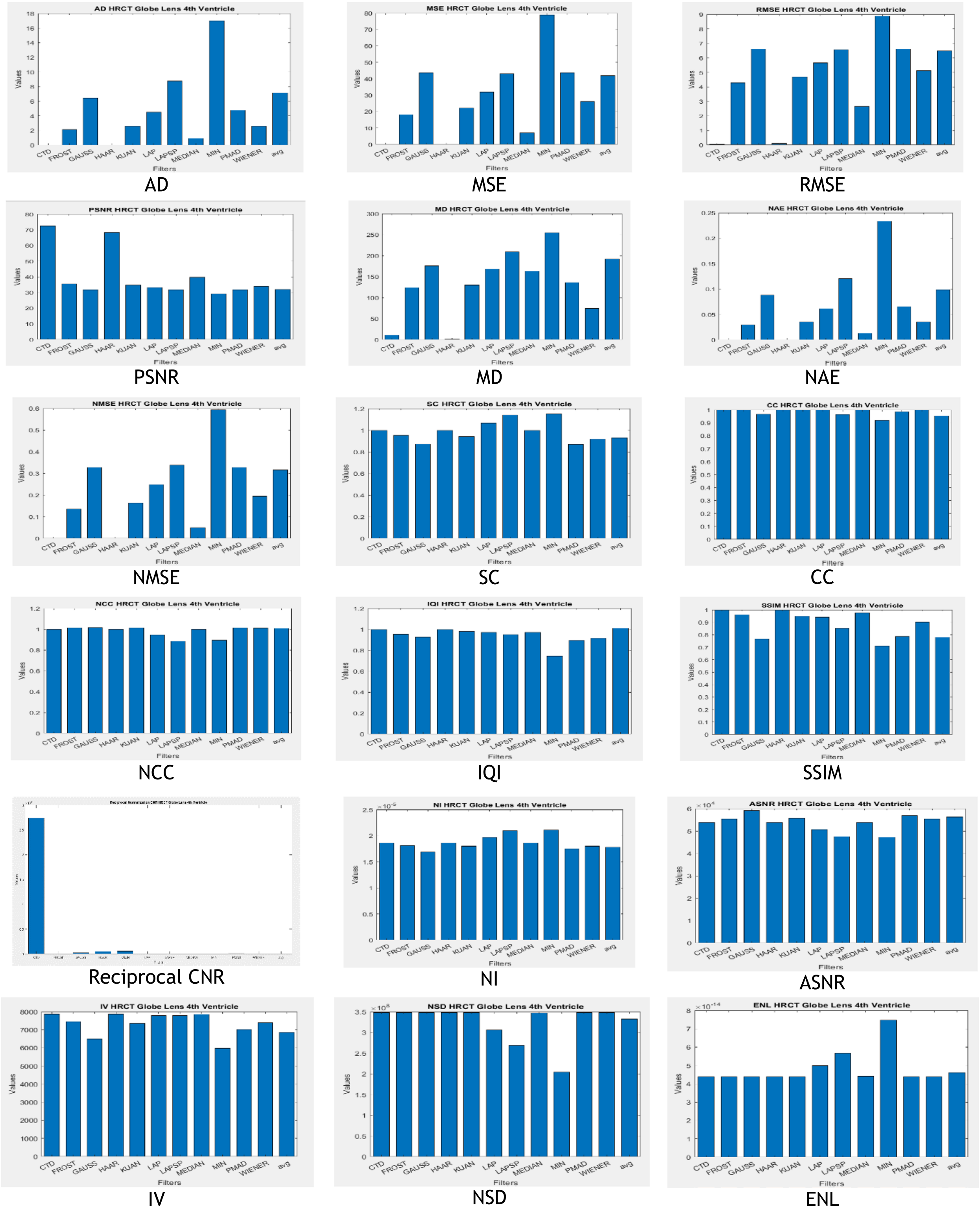

AD MSE RMSE

PSNR MD NAE

NMSE SC CC

NCC IQI SSIM

Reciprocal CNR NI ASNR

IV NSD ENL

Fig. 4 Histogram plots of the performance metrics of Globe Lens 4th Ventricle

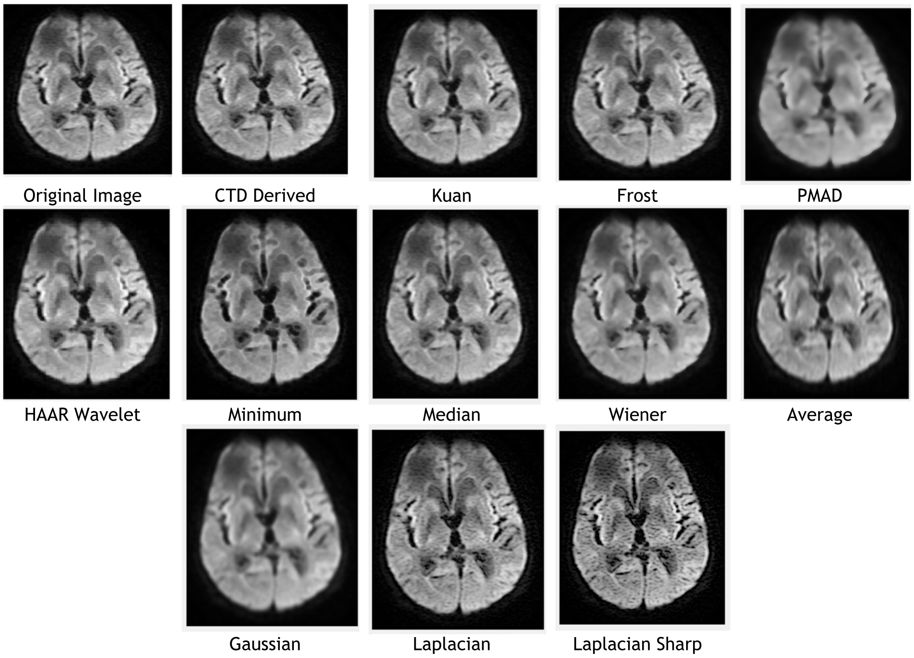

Fig. 5 Original and denoised Images of MCA DWI (B 800) MRI

improved visualization of the pyramidal structure of the fourth ventricle and enhanced details of the ocular globe, including its fibrous, vascular, and neural layers. The radiologist anticipates accurate detection of deformities and diseases by addressing hidden quantum mottle noise. The study focuses on CT images of the fourth ventricle, globe, and lens. Denoised images, including CTD and traditional filters, are presented in Fig. 3. The structurally preserved image will greatly assist ophthalmic surgeons and neuro-physicians in clinical treatment decisions, whether through surgery or non-invasive methods.

Observations from brain HRCT Globe Lens 4th Ventricle quality metrics and histogram plots (Table 4 and Fig. 4):

a. CTD filter yielded minimum values in AD, MSE, RMSE, MD, NAE, and NMSE, generating a high-quality denoised image useful for precise location identification and deformation needs in the globe, lens, and 4th ventricle, due to the selection efficiency of appropriate cost-function and subsequent computation of topological derivative.
b. Quality metrics SC, CC, NCC, IQI, and SSIM, indicators of shape and structure similarity, reached unity for CTD, highlighting its merit in retaining original shape and preserving structural details of aperture nature, unlike other traditional filters.
c. PSNR recorded a 50% higher value for CTD, demonstrating superior denoising ability over other filters, except Haar wavelet.
d. CNR, NI, ASNR, IV, NSD, and ENL values for CTD-filtered image surpassed those of other filters, ensuring fine contrast, noise-free, and radiologically preserved images for Globe-Lens 4th Ventricle.

Clinical example 3: MRI brain-middle cerebral artery territory DWI (B 800)

The Middle Cerebral Artery (MCA), the largest terminal branch of the internal carotid artery, supplies blood to the brain, traversing through distinct segments (M1 to M4). CT images reveal MCA segment discontinuity, while MR images disclose Circle of Willis anomalies. Radiologically, Moyamoya syndrome, aneursym formation, intracranial hemorrhage, and vascular variations differentiate rare rete MCA anomalies. Gaussian and Rayleigh noises in images may lead to misdiagnosis [130]. Besides, void signals in T2-MRI wittnessed in twig like MCA (T-MCA) for diagnoising hemodynmic delay, intracranial aneursym, internal carotid artery and

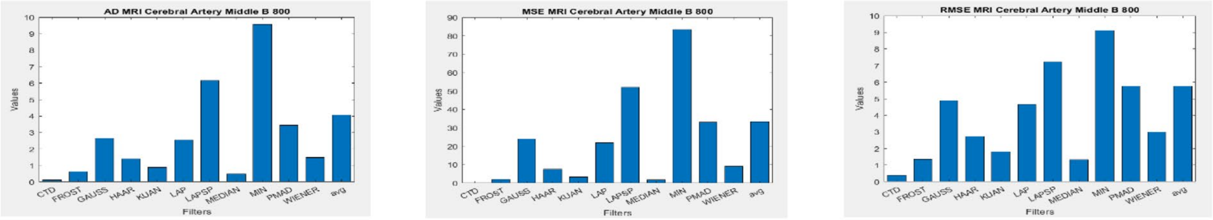

AD MSE RMSE

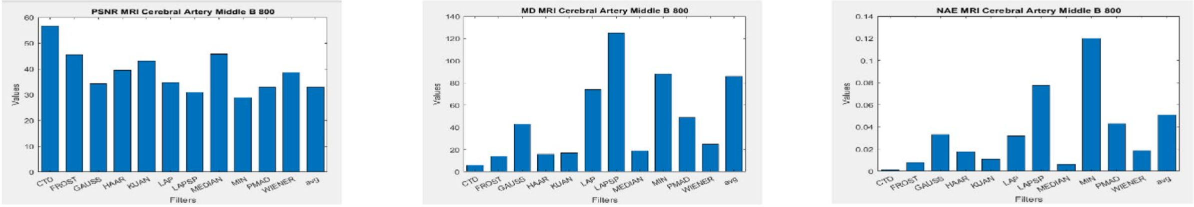

PSNR MD NAE

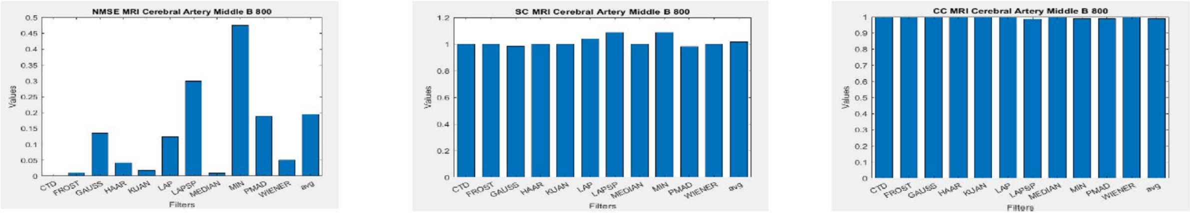

NMSE SC CC

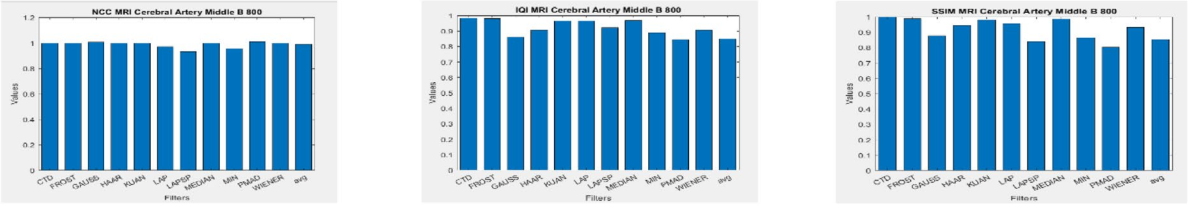

NCC IQI SSIM

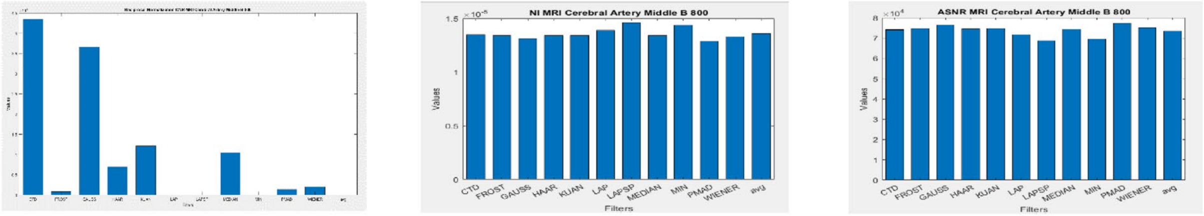

Reciprocal CNR NI ASNR

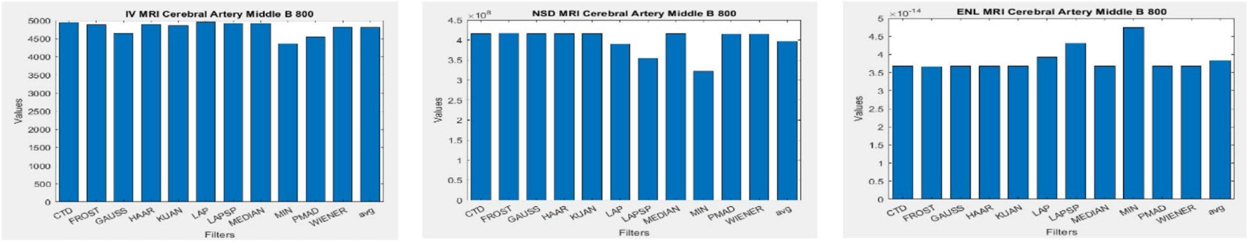

IV NSD ENL

Fig. 6 Histogram plots of the quality metrics for MCA DWI (B 800) MRI image trandsural anastomosis conditions in MCA is very difficult due to the presence of Gaussian and Raleigh's noises [131–137].

T-MCA anomalies are challenging due to void signals in T2-MRI, making Diffusion-weighted imaging (DWI) and Fluid-attenuated inversion recovery (FLAIR) essential. PROPELLER MRI reduces motion artifacts [138–140]. Despite advanced MRI modes, Gaussian and Rayleigh noises persist, necessitating denoising for accurate MCA diagnosis.

For Brain-MCA territory DWI (B 800) MRI, CTD and traditional filters were applied, displaying outputs in Fig. 5. Quality metrics and histogram plots are in Table 5 and Fig. 6. Radiologists noted CTD's distinguishable features in MCA territory, aiding easy detection of irregularities. Shape derivatives from CTD support neurologists in clinically and surgically assessing MCA abnormalities and severity.

Clinical example 4: MRI brain—middle cerebral artery territory FLAIR T2

Similarly, the Brain-MCA territory FLAIR T2 MR territory image underwent testing with both the proposed and traditional algorithms, as illustrated in Fig. 7. A summary of the quality metrics computed for all denoising algorithms is provided in Table 6, with their corresponding histogram plots displayed in Fig. 8. These results consistently demonstrate the effectiveness of the proposed CTD techniques in denoising.

Clinical example 5: MRI brain—middle cerebral artery territory PROP T2

Similarly, the Brain-MCA territory PROP T2 MR territory image underwent testing with various denoising algorithms, and the outcomes are illustrated in Fig. 9. Corresponding performance metrics and their histogram plots are detailed in Table 7 and Fig. 10, respectively. Altogether, following conclusions have been drawn for all of MCA territory MR images i.e., DWI (B 800), FLAIR T2 and PROP T2:

a. The CTD method, indicated by low scores in AD, MSE, RMSE, MD, NAE, and NMSE, strategically tuned the cost-function, effectively removing Gaussian and Rayleigh noises from Brain MCA territory DWI (B 800), FLAIR T2, and PROP T2 MR images. This denoising capability of the proposed CTD technique produces high-quality images crucial for assessing subtle changes in the MCA territory, quantifying injury severity accurately.
b. SC, CC, NCC, IQI, and SSIM, critical factors for similarity indices, consistently reached unity for CTD, indicating full retention of MCA territory after denoising. Deviations from the original MCA territory serve as strong indicators for acute stroke, accurately identified in CTD-filtered images, aiding physicians in detecting metastatic brain conditions in MCA regions.
c. PSNR returned noteworthy values for CTD, justifying its effectiveness in removing Gaussian and Ray-

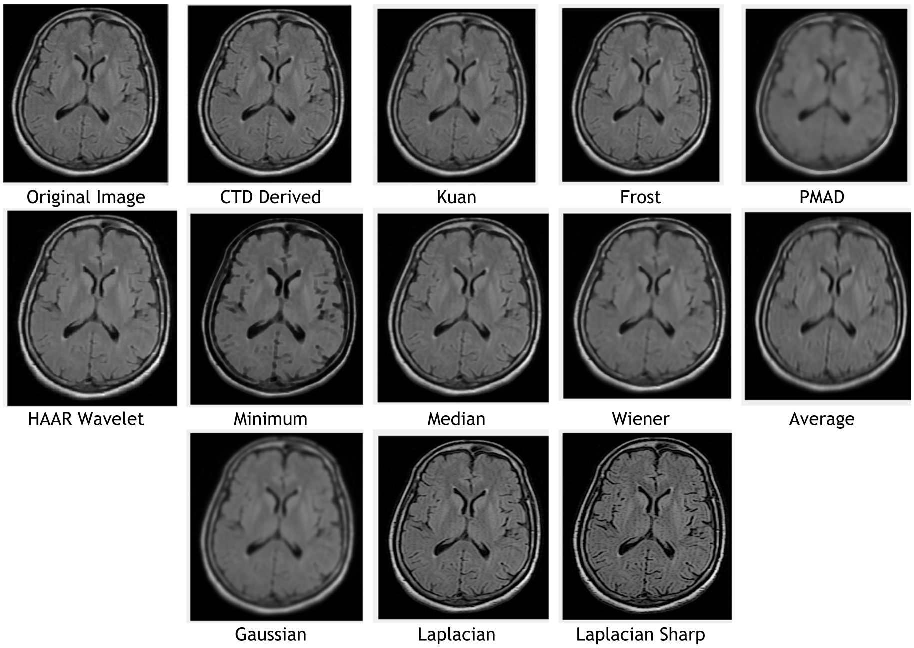

Fig. 7 Original and Denoised images of MRI MCA FLAIR T2

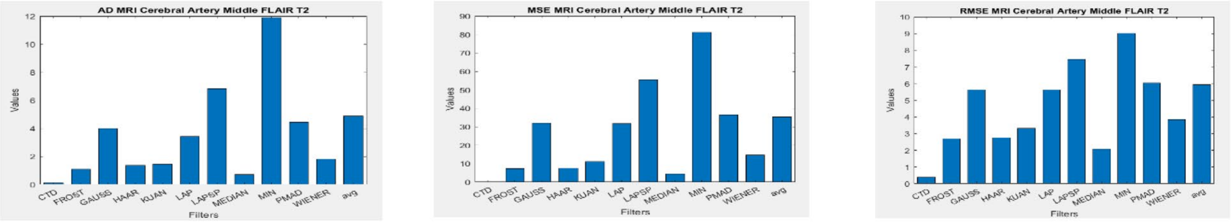

AD MSE RMSE

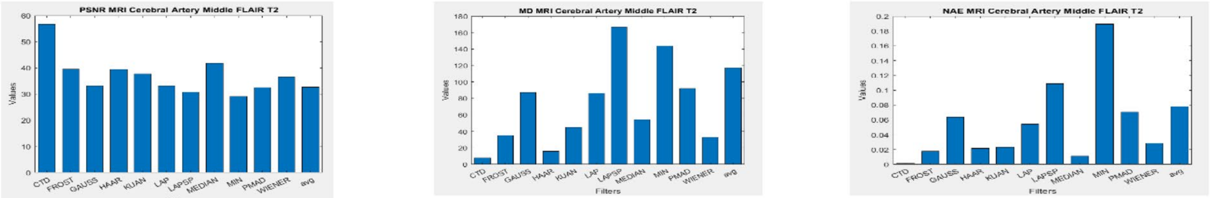

PSNR MD NAE

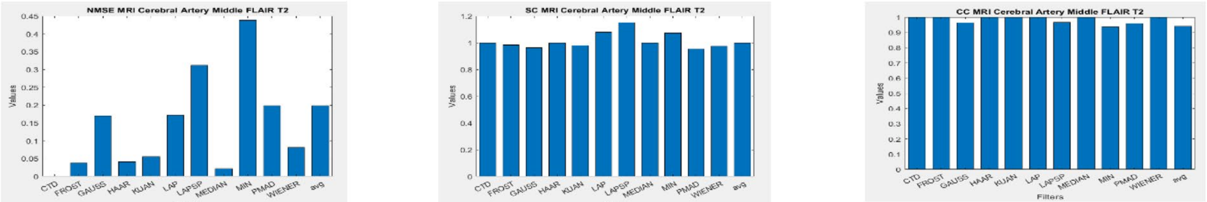

NMSE SC CC

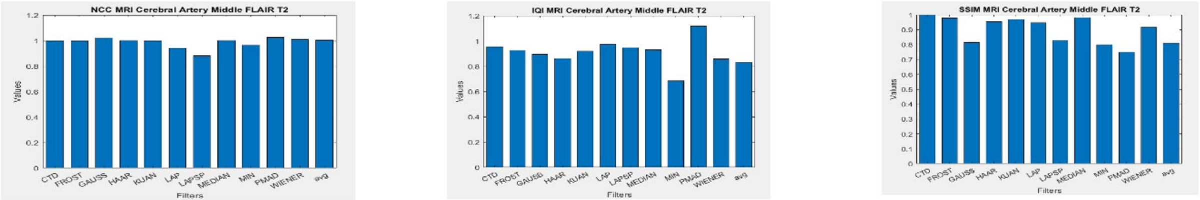

NCC IQI SSIM

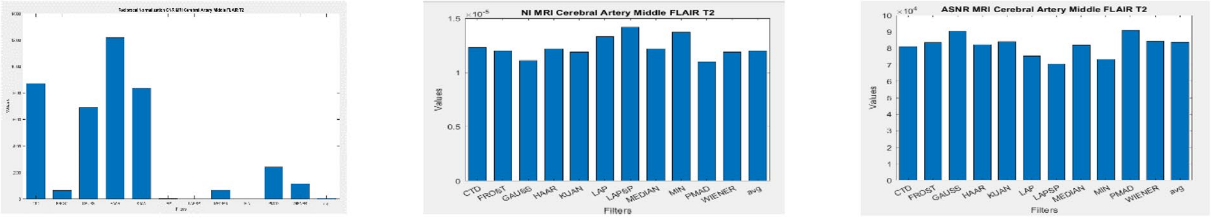

Reciprocal CNR NI ASNR

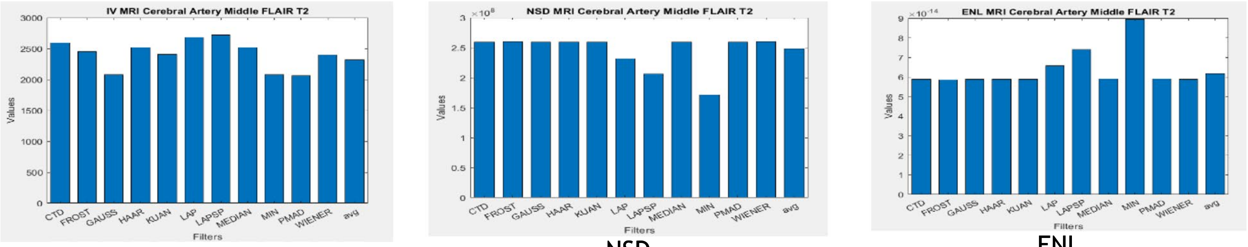

IV NSD ENL

Fig. 8 Histogram plots of the performance metrics for brain MCA FLAIR T2 MR Image

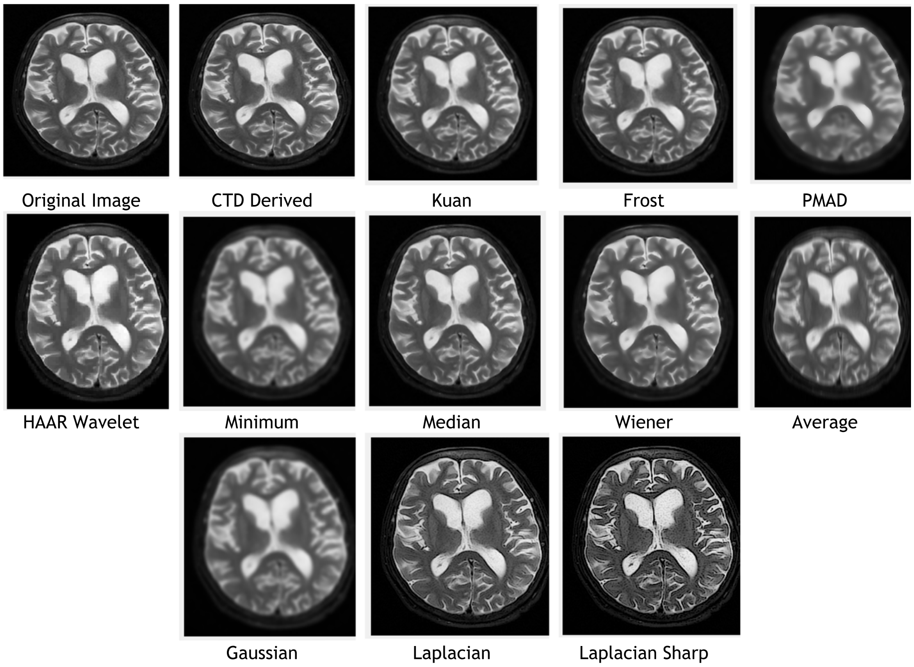

Fig. 9 Original and denoised images of MRI MCA PROP T2

leigh noise in MCA territory DWI (B 800), FLAIR T2 and PROP T2 MR images.

d. CNR, NI, ASNR, IV, NSD, and ENL metrics recorded noteworthy values for CTD, resulting in improved contrast, noise-free, and distinctly preserved territorial regions of MCA territory DWI (B 800), FLAIR T2, and PROP T2 MR images.

In all clinical examples (1–5), the relative residual value is extremely low, indicating that the CTD algorithm converges with a minimum number of iterations, generating negligible errors, and ensuring very good quality in denoised images. Further analysis of the CTD algorithm for diseased regions of MCA territory will be presented in clinical examples 6, 7, and 8 given below.

Clinical Examples 6, 7 and 8: Infarct and Demyelination

This section presents a detailed analysis of brain regions using CTD and other denoising filters (Figs. 11, 13, and 15). Performance metrics from these filters are reported in Tables 8, 9, and 10, with their distribution visualized in histogram plots (Figs. 12, 14, and 16). The results offer insights into the filters' effectiveness in improving image quality and detecting brain diseased region.

Figure 11 presents MR images obtained through DWI, known for its ability to provide excellent lesion contrast and differentiate strokes from conditions mimicking strokes. DWI identifies diffusion restriction, indicating acute infarct presence, and effectively visualizes cerebral infarction volume. It consistently delivers excellent results from early lesion stages to full infarction, aiding prognosis in stroke patients' follow-up scans.

DWI also detects vasogenic edema and acute lesions in chronic ischemic cases, offering insights into brain physiology. Notably, the CTD-derived acute infarct DWI image displayed exceptional quality, similarity, and noise metrics (Table 8, Fig. 12), emphasizing enhanced contrast and diffusion aspects. Thus, neuro physicians and radiologists can rely on CTD-enhanced images for accurate stroke detection and brain damage assessment.

The denoised images illustrate MR images obtained using the DWI technique, with various applied filters (Fig. 13). While DWI is commonly used for infarct cases, it plays a crucial role in identifying Ischemic Demyelination cases, distinguishing between vascular ischemia (restricted diffusion) and demyelination (facilitated diffusion). This sequence proves advantageous in characterizing tissue and histopathology in cases of ischemic

AD MSE RMSE

PSNR MD NAE

NMSE SC CC

NCC IQI SSIM

Reciprocal CNR NI ASNR

IV NSD ENL

Fig. 10 Histogram plots of the performance metrics of brain MCA PROP T2

demyelination disease. In this rare case, CTD demonstrated its uniqueness through performance values (Table 9) and histogram plots (Fig. 14). CTD-derived images excel in producing enhanced representations of demyelination diseases, showing a high degree of structural similarity (unit values for SC, CC, NCC, IQI, and

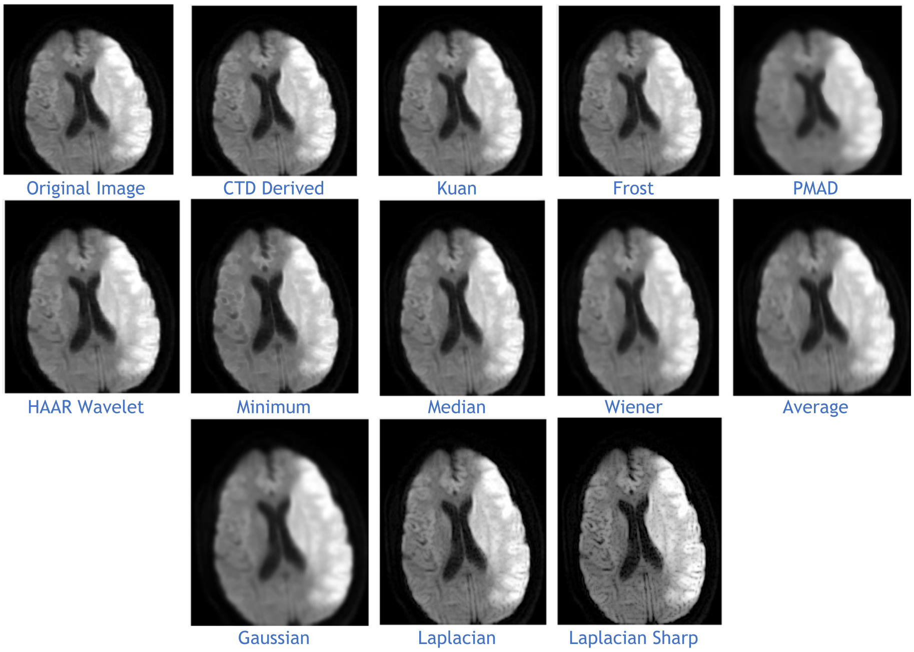
Original Image CTD Derived Kuan Frost PMAD
HAAR Wavelet Minimum Median Wiener Average
Gaussian Laplacian Laplacian Sharp

Fig. 11 Examination of Acute Infarct images obtained by application of various denoising filters

SSIM). This characteristic is critical when analyzing images with restricted diffusion.

Figure 15 displays MR images obtained using the DWI technique, processed with various denoising filters. DWI identifies ischemic changes in brain tissue, represented as hyperintensity in MR DWI images. Cerebral Small Vessel Disease (SVD), characterized by nil restricted diffusion, is an indicator for cerebral infarct. The CTD cerebral infarct image in Fig. 15 stands out for exceptional denoising quality, enhancing hyperintensity regions significantly, as indicated by the outstanding PSNR value. Minimal values in both quality and noise metrics (Table 10) and corresponding histogram plots (Fig. 16) affirm the effectiveness of this denoising approach. Additionally, the hyperintensity signals in this CTD image exhibit no noticeable distortion, underscoring the reliability and accuracy of the denoising process employed in generating the enhanced image.

Inferences from filtered images, metrics, and histogram plots for infarct and Ischemic Demyelination cases are outlined below:

Acute and Cerebral Infarct DWI:

a AD, MSE, RMSE, MD, NAE, and NMSE demonstrate remarkably low values compared to other filters, indicating effective denoising of Gaussian and Rayleigh noises. The CTD technique enhances hyperintense areas, delivering high-quality images for accurate brain infarct identification, showcasing superior denoising capabilities.

b SC, CC, NCC, and SSIM yield unity for CTD, with IQI slightly below unity, a unique characteristic. Other filters show metric values either lower or higher than unity, indicating that CTD retains similarity in infarct brain MRI images with high accuracy after denoising.

c The PSNR value for CTD surpasses other filters, showcasing its effectiveness in removing both foreground and background noise from diseased brain images.

d CNR, NI, ASNR, IV, NSD, and ENL metrics exhibit favorable values for CTD, ensuring enhanced contrast, noise-free results, and well-preserved radiological features in brain infarct MRI images.

Ischemic Demyelination Disease:

a AD, MSE, RMSE, MD, NAE, and NMSE show notably low values compared to other filters, indicating effective denoising of Gaussian and Rayleigh noises in the brain affected by Ischemic

AD MSE RMSE

PSNR MD NAE

NMSE SC CC

NCC IQI SSIM

Reciprocal CNR NI ASNR

IV NSD ENL

Fig. 12 Histogram plots of the performance metrics of acute cerebral infarct

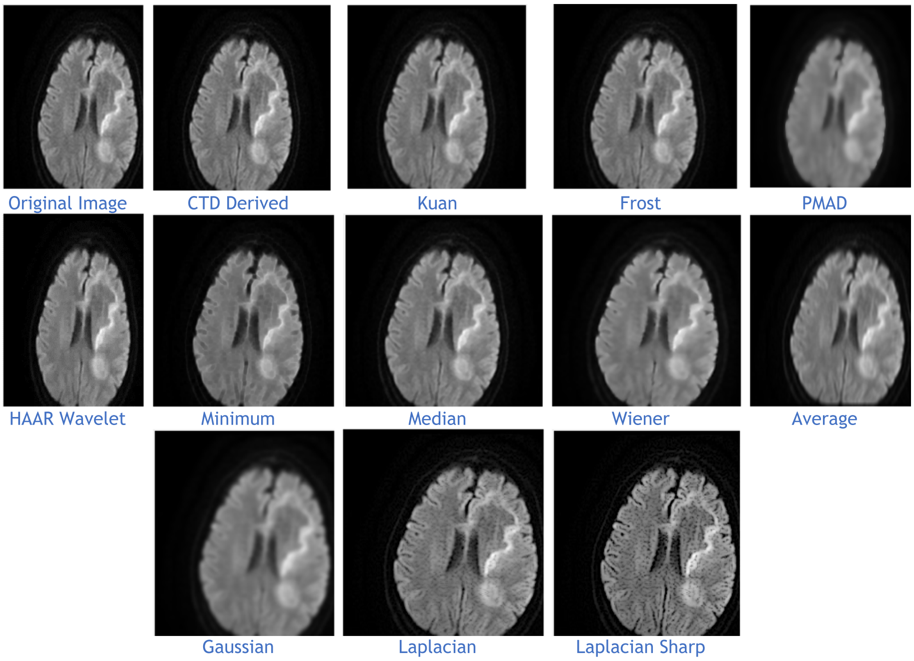

Fig. 13 Denoised images of the brain MRI of Ischemic Demyelination disease for various filters and the proposed CTD filter

Demyelination Disease. The CTD-derived MRI image differentiates hypo and hyper intense areas excellently, providing crucial information about demyelination and ischemic changes in the diseased brain.

b SC, CC, NCC, IQI, and SSIM all achieve unity for the CTD filter, while other filters show values greater than or less than unity. The CTD denoised image returns a highly structured image with zero error, enabling easy observation of subtle shifts in ischemic demyelination within the brain tissue.

c The PSNR returns an excellent value for the CTD filter, affirming its ability to address both foreground and background noise in diseased brain tissues effectively.

d The CNR, NI, ASNR, IV, NSD, and ENL metrics demonstrate outstanding values for the CTD-derived image, leading to improved contrast and radiologically preserved features in MR images of diseased brain tissues.

In conclusion, the CTD-filtered ischemic demyelination Brain MR image yields exceptional results, shedding further light on pathogenesis and enabling further evaluation of white matter lesions. This is evident through visual inspection and the estimated performance metrics.

Clinical Examples 9, 10 and 11: Neoplastic lesions

To comprehensively evaluate the efficacy of CTD and denoising filters, our study expands to encompass cases of cerebral neoplasms. The brain exhibits various neoplastic lesions, including gliomas, glioblastoma, choroid plexus tumors, anaplastic astrocytoma, fibrillary astrocytoma, meningioma, cerebellar medulloblastoma, oligodendroglioma, craniopharyngioma, pituitary adenomas, brain metastases, and CNS lymphomas [141]. Accurate detection and differentiation of neoplastic lesions, crucial in neuroscience research, also include Neurofibromatosis type 1 [142] and multiple ring-enhancing lesions [143]. Dynamic contrast-enhanced MRI effectively distinguishes neoplastic lesions [144]. Gliomas, predominantly found in the central nervous system, often necessitate biopsy for verification, with altered metabolic activity and SSADH expression significantly influencing their growth [145, 146]. Note that gliomas are considered malignant [147].

4th ventricular tumors, strongly associated with spine metastases (SM), play a vital role in cerebral neoplasm identification [148]. Leptomeningeal disease (LMD) is common in cerebellar medulloblastomas, a specific neoplasm [149]. Rare cerebral neoplasms like Rosette-forming glioneuronal tumors (RGNT) occur in the 4th ventricle [150]. Treatment options for RGNT include gamma knife radiosurgery [151], azacytidine [152, 153],

AD MSE RMSE

PSNR MD NAE

NMSE SC CC

NCC IQI SSIM

Reciprocal CNR NI ASNR

IV NSD ENL

Fig. 14 Histogram plots of the performance metrics of Ischemic Demyelination Disease

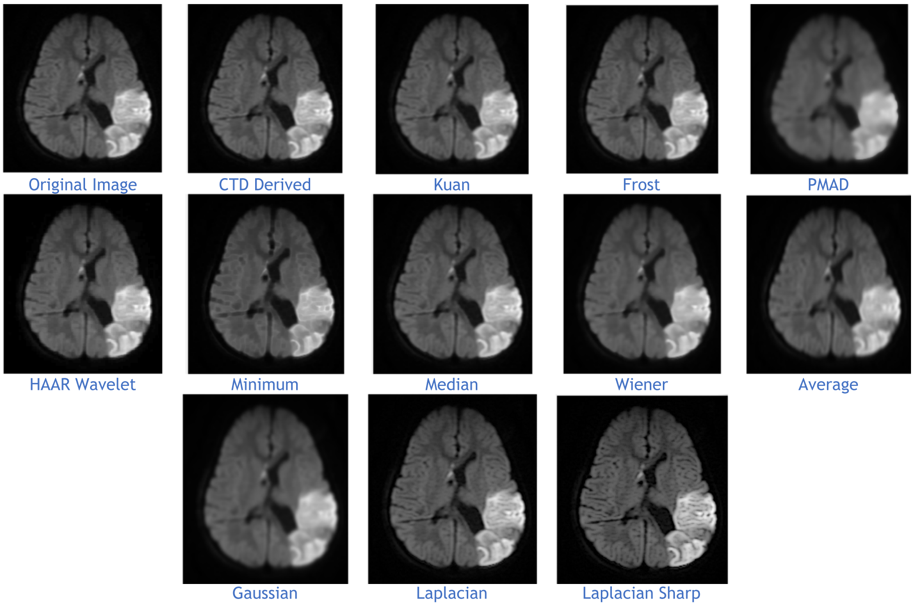

Fig. 15 Denoised output images of cerebral infarct disease of different types of filters and the CTD filter

staged open cranial surgery [154], and tumor resection [155, 156], effectively managing and treating cerebral neoplasms.

Glioma lesions pose challenges for clinical diagnosis and imaging interpretation due to their neoplastic nature. This study highlights the use of MRI PROP mode for identifying neoplastic glioma lesions, chosen for its exceptional imaging capabilities crucial for tackling such lesions. Distinguishing between neoplasms and other conditions in MRI can be daunting, but PROP MRI, with glioma lesions manifesting as abnormal or high-intensity signals, aids in differentiation and contributes significantly to histopathological studies.

The CTD-derived image (Fig. 17) proves highly beneficial in glioma analysis, offering high denoising value while genuinely preserving the original image signal and enhancing its quality. Quality and similarity metrics scores for the CTD image are impressive, as seen in metric values (Table 11) and corresponding histogram plots (Fig. 18). The nature and structural preservation in CTD images remain consistently striking for all glioma grades.

The combination of MRI PROP mode and CTD-derived images demonstrates a promising approach for accurate glioma diagnosis, supporting improved patient care and outcomes. CTD's crystal-clear imaging and denoising advantages provide valuable support to clinicians and radiologists in detecting and characterizing glioma neoplastic lesions effectively.

Once again, we've selected an MR PROPELLER image, emphasizing PROP mode's exceptional ability to display high-quality images crucial for neoplastic cases. The focus is on creating a clear MRI environment for comparing different neoplastic lesion cases, particularly challenging cases like 4th ventricular tumors. These intraventricular tumors, situated within the ventricular cavity, pose a difficulty in accurate detection.

This study presents two distinct neoplastic tumor cases in PROP mode (Figs. 17 and 19). Applying the CTD algorithm to these already clear images returns unparalleled results, showcasing its exceptional performance across various diseased cases. Despite a slight decrease in PSNR compared to glioma lesions, this is valuable as radiological signatures can be weak for 4th ventricular neoplastic tumors.

Comparatively, quality and similarity metrics in CTD images closely align with glioma neoplastic lesions, evident in quality metric values (Table 12) and histogram plots (Fig. 20). Like in other cases, the CTD image preserves structural similarity, consistently producing enhanced radiological images.

In summary, the combination of MR PROPELLER and the CTD algorithm proves a powerful and reliable approach for neoplastic lesion imaging. Providing high-quality and detailed images, this combination aids radiologists in effectively detecting and analyzing neoplastic lesions, especially challenging 4th ventricular

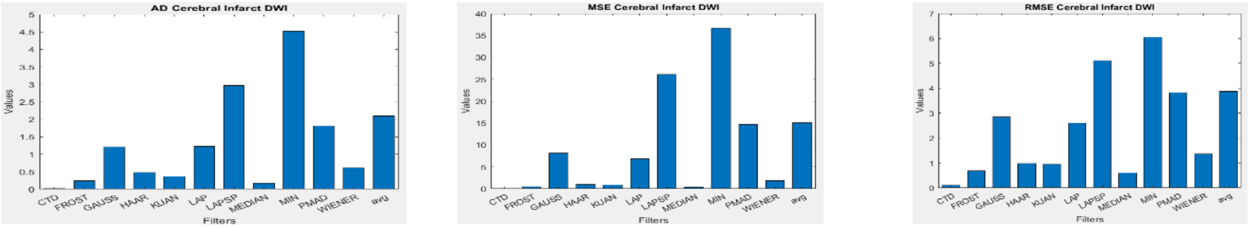

AD MSE RMSE

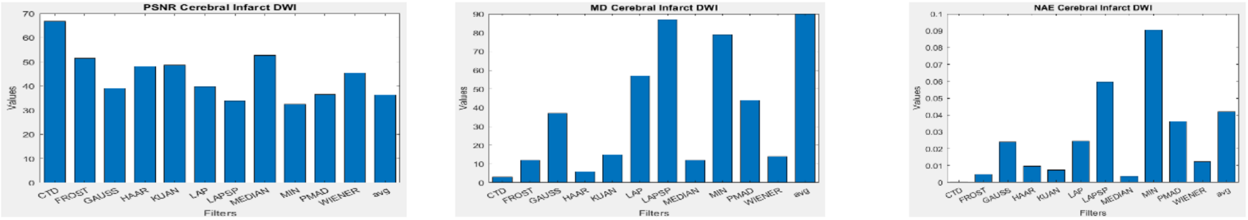

PSNR MD NAE

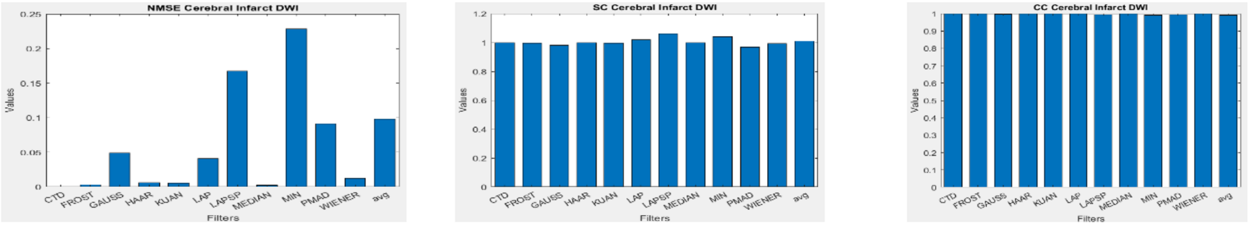

NMSE SC CC

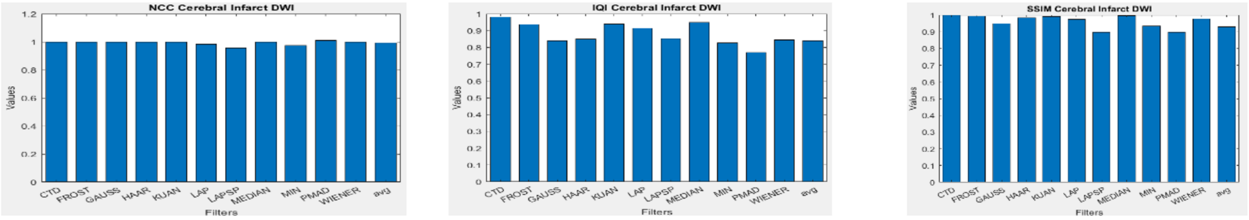

NCC IQI SSIM

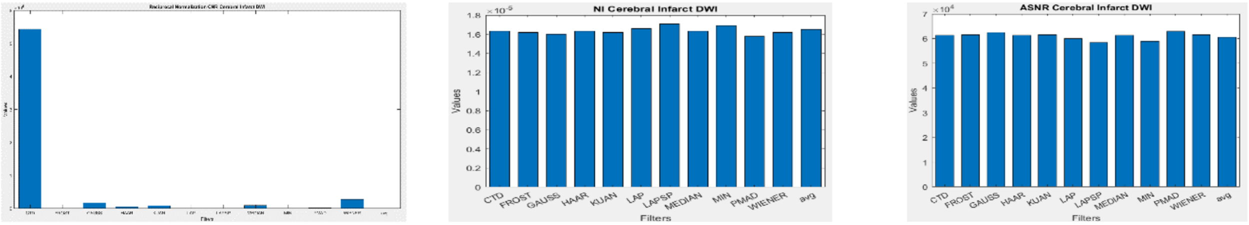

Reciprocal CNR NI ASNR

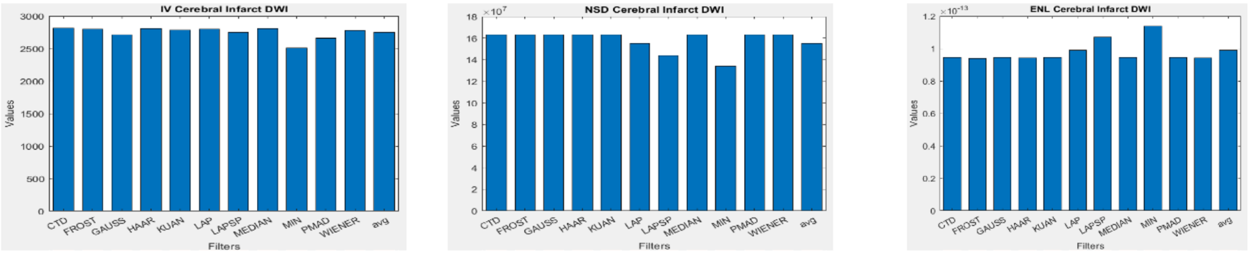

IV NSD ENL

Fig. 16 Histogram plots of the performance metrics of cerebral infarct

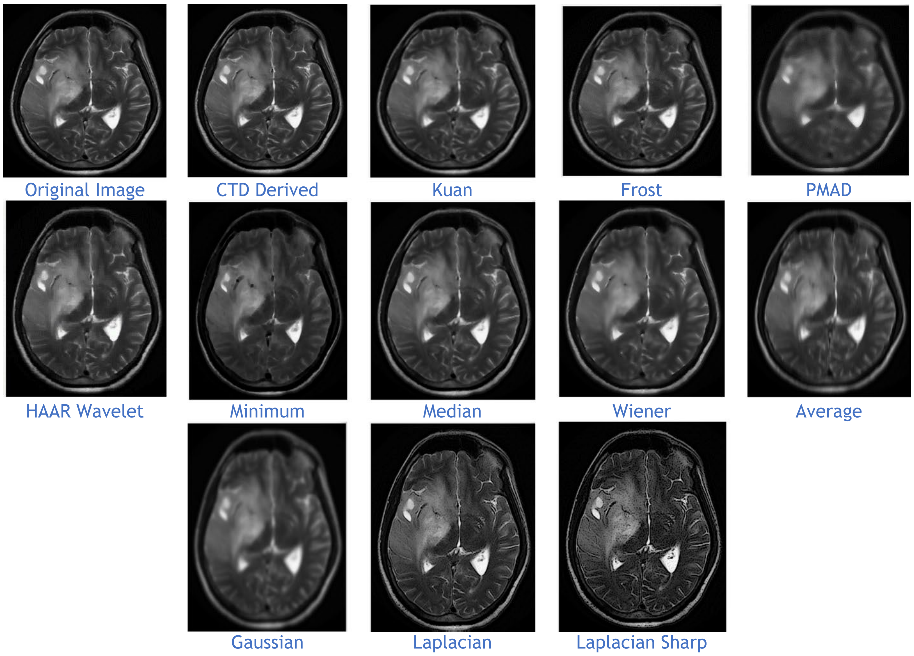

Fig. 17 Denoised images of glioma neoplastic lesion as observed in the upper left corner

tumors within the ventricular cavity. The CTD algorithm's exceptional performance solidifies its position as a valuable tool for enhancing radiological images across various diseased conditions.

In this study, FLAIR MRI is chosen for its ability to delineate gliomas, offering excellent multiplanar structural information and enhanced tissue characterization. A comparison between FLAIR and PROP mode reveals distinct strengths in detecting neoplastic lesions. FLAIR MRI excels in providing valuable structural information for gliomas, contributing to their diagnosis and prognosis.

Practical analysis highlights clear differences in CTD-derived images from PROP (Fig. 17) and FLAIR (Fig. 21) sequences for gliomas. Notably, PROP displays higher signal intensity features, while FLAIR exhibits diminished features. Despite variations, the CTD-derived FLAIR image demonstrates commendable denoising, ensuring a distortion-free image, supported by the PSNR value.

Structural similarity (Table 13) and noise metrics histogram plots (Fig. 22), yield good values, though not as high as PROP, affirming radiologically well-preserved and error-free characteristics in the CTD FLAIR image. Both FLAIR and PROP MRI sequences prove valuable for glioma detection, with the CTD FLAIR image remaining a robust resource for accurate evaluation and analysis despite slight metric differences between the two sequences.

Based on the analysis of neoplastic lesion cases, the following conclusions were drawn:

a. The CTD algorithm effectively removed Gaussian and Rayleigh noises, resulting in superior denoised images crucial for identifying cerebral edema in neoplastic brain lesions.
b. Metrics such as SC, CC, NCC, and SSIM consistently showed a unity value for the CTD filter, maintaining striking similarity in neoplastic brain MR images. Even with greater denoising accuracy, the CTD image retained similarity, especially in cases involving blood vessel infiltration, compression, or vasospasm associated with cerebral neoplasms.
c. The PSNR value for the CTD filter exceeded expectations, confirming its remarkable noise removal capability in neoplastic brain MR images.
d. Metrics like CNR, NI, ASNR, IV, NSD, and ENL demonstrated commendable values for the CTD image, resulting in exceptional neoplastic brain MR images with enhanced contrast and well-preserved radiological features. This contributes to improved clinical diagnosis in various areas.

AD MSE RMSE

PSNR MD NAE

NMSE SC CC

NCC IQI SSIM

Reciprocal CNR NI ASNR

IV NSD ENL

Fig. 18 Histogram plots of the performance metrics of Neoplastic Lesion 1 glioma

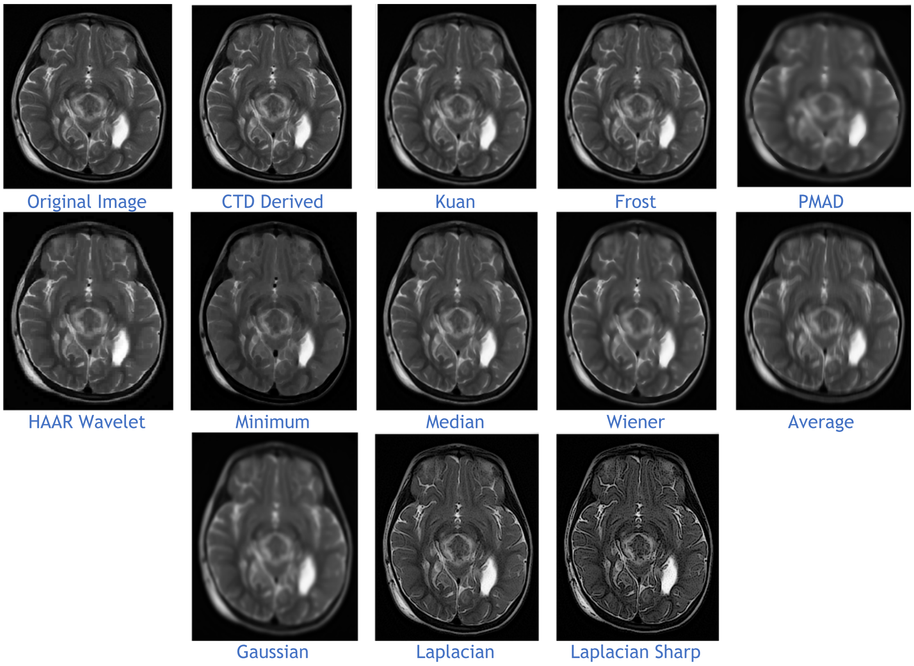

Fig. 19 Denoised images of 4th ventricle tumour, a rare case of neoplastic lesion

e. Overall, the CTD filtered neoplastic brain MRI provided noise-free images with maintained structural similarity, as confirmed through visual inspection and estimated performance metrics.

Results

The proposed CTD filter and other filters were assessed on various CT and MR images, and key inferences were drawn:

a. Gaussian filter, while moderate in denoising, lacks efficient edge and contour preservation.
b. Wiener denoising filter, despite suppressing frequency components, falls short in efficient edge and contour filtering.
c. Laplacian filter, a derivative-based method, excels in preserving edge and contour details but results in loss of tissue-based information.
d. Laplacian Sharp filter, another derivative-based method, preserves edge and contour details but lacks expected reliability in contrast details.
e. Average filter, a denoising technique, yields poor results while preserving edges and contours.
f. Minimum filter, a poor denoising filter, struggles to preserve edges and contours.
g. Median filter, an average denoising filter, moderately preserves edges and contours.
h. PMAD, a diffusion-based filter, performs moderately but shows poor denoising at edges and contours without loss in details.
i. Kuan filter, a statistical-based technique, achieves modest performance in denoising and contrast enhancement.
j. Frost filter, an exponential-based method, performs at a medium level in improving denoising and contrast.
k. Haar, a wavelet-based filter, offers optimum performance in denoising, edge and contour preservation, and contrast enhancement.
l. The proposed CTD filter is validated as the best choice for denoising, showcasing commendable performance in denoising, structural preservation of edges and contours, and contrast enhancement. Further, the visual inspection and estimated performance metrics affirm the denoising abilities of the proposed CTD filter substantiated by quality improvements

AD MSE RMSE

PSNR MD NAE

NMSE SC CC

NCC IQI SSIM

Reciprocal CNR NI ASNR

IV NSD ENL

Fig. 20 Histogram plots of the performance metrics of Neoplastic Lesion 2—4th ventricle tumour

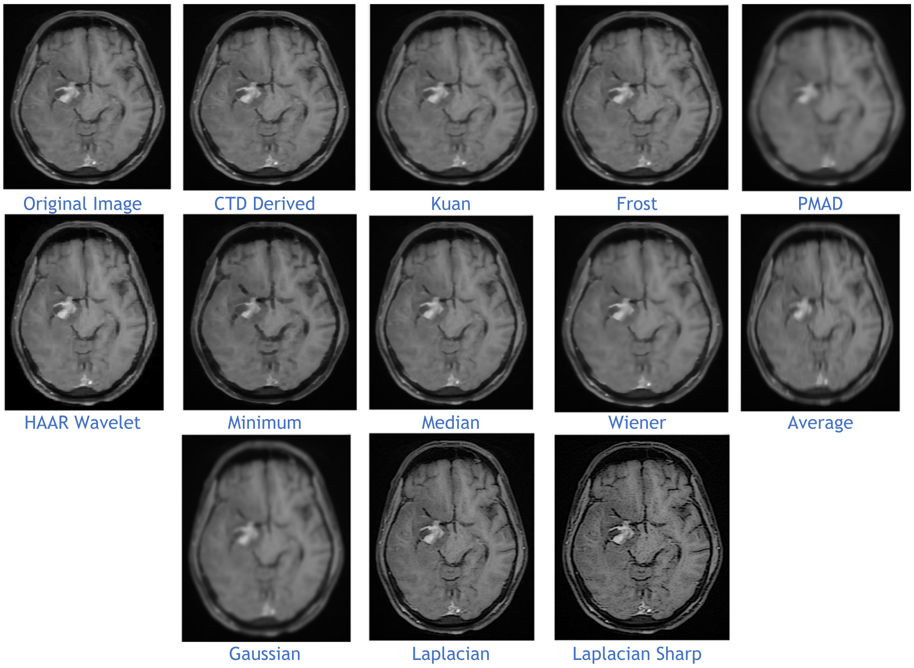

Fig. 21 Denoised images of glioma lesion seen in middle left region of brain

across all CT and MR test images (clinical examples 1–11) in this research study.

Discussion

Biomedical imaging modalities like CT and MRI are prone to noise and artifacts, which impacting image quality. Our research focused on the CTD technique, addressing quantum mottle noise in CT and Gaussian/Rayleigh noises in MR images. CTD excelled by achieving infinitesimal residual values with fewer iterations and shape functionality, outperforming traditional filters. Comparative studies, case analyses, visual inspections, and metrics affirmed CTD's superiority, making it a valuable tool for future medical imaging assessments.

Furthermore, the CTD algorithm proved to be a robust computational technique for addressing critical visual aspects, such as similarity checks, contrast issues, and delineation of boundaries in both normal and pathological CT and MR images. Although the noise metrics scored similarly with respect to other filters, the CTD technique consistently achieved better values, thus demonstrating its overall superiority. Altogether CTD provided a clear picture of ridge shape, articulate globe lens with excellent clarity, distinct contrast of MCA territory, access the damage caused in MCA territory under various diseased conditions, improved resolution over hypo and hyper intense regions in all the cases of HRCT, CT and MR images including the diseased ones. The algorithm proved robust, addressing visual aspects and providing clarity in both normal and pathological images. CTD consistently surpassed other techniques in noise metrics, offering enhanced resolution in HRCT, CT, and MR images. Despite its longer execution time (5–7 min), CTD's clinical validity and lack of major drawbacks reinforce its potential for high-quality image delivery.

Conclusion

CT and MRI are standard imaging modalities but struggle with inherent noises, like quantum mottle in CT and Rayleigh, Rician, and Gaussian noises in MRI, impacting diagnostic clarity. Existing techniques fall short in fully addressing these issues. This research introduces the CTD framework, effectively mitigating noise problems in both CT and MRI. The outcomes of this research are profoundly encouraging and hold significant potential for acquiring precise diagnostic insights, especially in critical cases like Thoracic Cavity Carina, Head CT Globe Lens 4th Ventricle, Brain-Middle Cerebral Artery Territory, and neoplastic lesions. These discoveries establish the groundwork for integrating the

AD MSE RMSE

PSNR MD NAE

NMSE SC CC

NCC IQI SSIM

Reciprocal CNR NI ASNR

IV NSD ENL

Fig. 22 Histogram plots of the performance metrics of Neoplastic Lesion Ax T1 FLAIR glioma proposed CTD technique into standard clinical diagnostic practices.

Comparative studies, clinical examples, visual inspections, and performance metrics confirm CTD's superiority over traditional filters. CTD holds promise for Computer-Aided Diagnosis (CAD) post field trials. The results inspire confidence in accurate diagnostics for critical cases, setting the stage for routine clinical use. However, CTD's complex nature hinders real-time implementation, prompting future exploration of hardware deployment in FPGA/Raspberry Pi/Arduino for thorough testing and validation in real-world scenarios.

Abbreviations

CT	Computer Tomography
HRCT	High Resolution Computed Tomography
MRI	Magnetic Resonance Imaging
T1, T2	Relaxation times
FLAIR	Fluid Attenuated Inversion Recovery
DWI	Diffusion Weighed Imaging
PROPELLER	Periodically Rotated Overlapping Parallel Lines with Enhanced Reconstruction
FBP	Filtered Back Projection
SAFIRE	Sinogram Affirmed Iterative Reconstruction
AD	Average Difference
MSE	Mean Square Error
RMSE	Root Mean Square Error
MD	Maximum Difference
NAE	Normalized Absolute Error
NMSE	Normalized Mean Square Error
PSNR	Peak Signal to Noise Ratio
SC	Structural Content
CC	Correlation Coefficient
NCC	Normalized Cross Correlation
IQI	Image Quality Index
SSIM	Structural Similarity Index Map
CNR	Contrast to Noise Ratio
NI	Noise Index
ASNR	Average Signal to Noise Ratio
IV	Image Variance
NSD	Noise Standard Deviation
ENL	Equivalent Number of Looks
TD	Topological Derivative
CTD	Continuum Topological Derivative
DFB	Discrete Filter Bank
CLT	Contourlet Transform
PDFB	Pyramidal Directional Filter Bank
EIT	Electrical Impedance Tomography
DICOM	Digital imaging and communication system
PACS	Picture Archiving and Communication System
RIS	Radiology Information Systems
DFOV	Display Field of View
SPI	Spiral mode
MCA	Middle Cerebral Artery
T-MCA	Twig like MCA
CAD	Computer Aided Diagnosis
SSADH	Succinic Semialdehyde Dehydrogenase
SM	Spine Metastases
LMD	Leptomeningeal Disease
RGNT	Rosette-forming glioneuronal Tumor
TIA	Transient Ischemic Attack
CADASIL	Cerebral Autosomal Dominant Arteriopathy with Subcortical Infarcts and Leukoencephalopathy
SVD	Small Vessel Disease

Supplementary Information

The online version contains supplementary material available at https://doi.org/10.1186/s12880-024-01341-1.

Supplementary Material 1.
Supplementary Material 2.
Supplementary Material 3.
Supplementary Material 4.
Supplementary Material 5.
Supplementary Material 6.
Supplementary Material 7.
Supplementary Material 8.
Supplementary Material 9.
Supplementary Material 10.
Supplementary Material 11.
Supplementary Material 12.
Supplementary Material 13.
Supplementary Material 14.

Acknowledgements

My sincere thanks to Central Instrumentation and Service Lab (CISL), Guindy campus, University of Madras for providing all kind of support regarding this research work

Authors' contributions

Conceptualization, methodology, and Correction of the full manuscript were done by DN. Algorithm Development, Data Collection, testing and validation were carried by MV. Visual inspection and Diagnostic details were provided by SJ. All authors read and approved the final manuscript.

Funding

No funding.

Availability of data and materials

The medical image data required for this research work on CT and MRI images was generously provided by Image Art, Vijaya Health Centre, located in Vadapalani, Chennai. We express our gratitude for their invaluable contribution.
It is important to note that patient data will only be shared on an individual request basis, after ensuring compliance with the ethical conditions set by the data provider. The datasets utilized in this research article, along with the supplementary files, are included and made available for reference.

Declarations

Ethics approval and consent to participate

All clinical example were carried out by following the relevant guidelines. No treatment was practised, no data were gathered for management of patients, and no diagnostic information was taken from patients while developing the algorithm. None of the medical image data were passed on to surgeon or to any radiologist for surgery or diagnosis of diseases when testing the algorithms. Since the algorithm developed and tested in this research article does not involve medical image data directly from patients in any form, there is no need for consent form. The medical image datasets used in this research article were provided to us from an already available CT and MRI database in PACS, Image Art, Vijaya Health Centre, Vadapalani, Chennai, which is a cloud-based system.

Consent for publication

Not applicable.

Competing interests

The authors declare no competing interests.

Author details
[1]Central Instrumentation & Service Laboratory, Guindy Campus, University of Madras, Chennai, India. [2]Image Art, Vijaya Health Centre, Vadapalani, Chennai, India.

Received: 28 February 2023 Accepted: 18 June 2024
Published online: 24 July 2024

References

1. Doi K. Diagnostic imaging over the last 50 years: research and development in medical imaging science and technology. Phys Med Biol. 2006;51(13):R5. https://doi.org/10.1088/0031-9155/51/13/R02.
2. Ritter F, Boskamp T, Homeyer A, Laue H, Schwier M, Link F, Peitgen HO. Medical image analysis. IEEE Pulse. 2011;2(6):60–70. https://doi.org/10.1109/MPUL.2011.942929.
3. Ota H, Takase K, Igarashi K, Chiba Y, Haga K, Saito H, Takahashi S. MDCT compared with digital subtraction angiography for assessment of lower extremity arterial occlusive disease: importance of reviewing cross-sectional images. Am J Roentgenol. 2004;182(1):201–9. https://doi.org/10.2214/ajr.182.1.1820201.
4. Loevner LA, Sonners AI, Schulman BJ, Slawek K, Weber RS, Rosenthal DI, Moonis G, Chalian AA. Reinterpretation of cross-sectional images in patients with head and neck cancer in the setting of a multidisciplinary cancer center. Am J Neuroradiol. 2002;23(10):1622–6 PMID: 12427610.
5. Lee S, Fichtinger G, Chirikjian GS. Numerical algorithms for spatial registration of line fiducials from cross-sectional images. Med Phys. 2002;29(8):1881–91. https://doi.org/10.1118/1.1493777.
6. Dong Z, Wu X, Ma Z. Research on 3D model reconstruction based on a sequence of cross-sectional images. Mach Vis Appl. 2021;32(4):1–6. https://doi.org/10.1007/s00138-021-01220-7.
7. Stark H, Woods J, Paul I, Hingorani R. Direct Fourier reconstruction in computer tomography. IEEE Trans Acoust Speech Signal Process. 1981;29(2):237–45. https://doi.org/10.1109/TASSP.1981.1163528.
8. Lynch DA, Godwin JD, Safrin S, Starko KM, Hormel P, Brown KK, Raghu G, King TE Jr, Bradford WZ, Schwartz DA, Webb WR. High-resolution computed tomography in idiopathic pulmonary fibrosis: diagnosis and prognosis. Am J Respir Crit Care Med. 2005;172(4):488–93. https://doi.org/10.1164/rccm.200412-1756OC.
9. Grenier P, Cordeau MP, Beigelman C. High-resolution computed tomography of the airways. J Thorac Imaging. 1993;8(3):213–29. https://doi.org/10.1097/00005382-199322000-00006.
10. Mayo JR. High resolution computed tomography, technical aspects. Radiol Clin North Am. 1991;29(5):1043–9 PMID: 1871254.
11. Balmer BD, Blüthgen C, Bässler B, Martini K, Huber FA, Ruby L, Schönenberger A, Frauenfelder T. Influence of CT image matrix size and kernel type on the assessment of HRCT in patients with SSC-ILD. Diagnostics. 2022;12(7):1662. https://doi.org/10.3390/diagnostics12071662.
12. Lustig M, Donoho DL, Santos JM, Pauly JM. Compressed sensing MRI. IEEE Signal Process Mag. 2008;25(2):72–82. https://doi.org/10.1109/MSP.2007.914728.
13. Solomon J, Samei E. Quantum noise properties of CT images with anatomical textured backgrounds across reconstruction algorithms: FBP and SAFIRE. Med Phys. 2014;41(9):091908. https://doi.org/10.1118/1.4893497.
14. Li X, Samei E. Comparison of patient size-based methods for estimating quantum noise in CT images of the lung. Med Phys. 2009;36(2):541–6. https://doi.org/10.1118/1.3058482.
15. Latifi K, Huang TC, Feygelman V, Budzevich MM, Moros EG, Dilling TJ, Stevens CW, van Elmpt W, Dekker A, Zhang GG. Effects of quantum noise in 4D-CT on deformable image registration and derived ventilation data. Phys Med Biol. 2013;58(21):7661. https://doi.org/10.1088/0031-9155/58/21/7661.
16. Park K, Lee HS, Lee J. Hybrid filter based on neural networks for removing quantum noise in low-dose medical X-ray CT images. Int J Fuzzy Logic and Intell Syst. 2015;15(2):102–10. https://doi.org/10.5391/IJFIS.2015.15.2.102.
17. Zhang A, Jiang H, Ma L, Liu Y, Yang XA. Shearlet-based algorithm for quantum noise removal in low-dose CT images. In: Medical Imaging 2016: Image Processing (Vol. 9784). SPIE; 2016. p. 972-978. https://doi.org/10.1117/12.2216562.
18. Yang YQ, Nakamori N, Yoshida Y. Improvement of CT image degraded by quantum mottle using singularity detection. IEICE Trans Inf Syst. 2003;86(1):123–30.
19. Wang L, Lu J, Li Y, Yahagi T, Okamoto T. Noise removal for medical X-ray images in wavelet domain. Electr Eng Jpn. 2008;163(3):37–46. https://doi.org/10.1002/eej.20486.
20. Gomi T, Nakajima M, Umeda T. Wavelet denoising for quantum noise removal in chest digital tomosynthesis. Int J Comput Assist Radiol Surg. 2015;10(1):75–86. https://doi.org/10.1007/s11548-014-1003-2.
21. Shih CT, Chang SJ, Liu YL, Wu J. Noise reduction of low-dose computed tomography using the multi-resolution total variation minimization algorithm. In: Medical Imaging 2013: Physics of Medical Imaging (Vol. 8668). SPIE. 2013. p. 680-688. https://doi.org/10.1117/12.2007543.
22. Yang YQ, Nakamori N, Yoshida Y, Tsunoo T, Endo M, Sato K. Denoising of cone beam CT image using wavelet transform. In: Medical Imaging 2002: Image Processing (Vol. 4684). 2002. p. 1077–1084. https://doi.org/10.1117/12.467064.
23. Chen B, Ning R. Cone-beam volume CT breast imaging: wavelet analysis-based multi-resolution reconstruction and de-noising technique. In: Medical Imaging 2002: Physics of Medical Imaging (Vol. 4682). SPIE. 2002. p. 236–244, (Vol. 4682, p. 236–244). https://doi.org/10.1117/12.465564.
24. Park JD, Huh Y, Jin SO, Jeon SC. Noise reduction of medical X-ray image using wavelet threshold in cone-beam CT. J Inst Electr Eng Korea SC. 2007;44(6):42–8.
25. Chan CL, Sullivan BJ, Sahakian AV, Katsaggelos AK, Frohlich T, Byrom E. Spatiotemporal filtering of digital angiographic image sequences corrupted by quantum mottle. In: Biomedical Image Processing II 1991 (Vol. 1450). SPIE; 1991. p. 208-217. https://doi.org/10.1117/12.44297.
26. Ohta M, Ikuta A, Mitani Y, Kodera Y, Ogawa M, Fujita M, Wada T. A new restoration method for medical X-ray images with optical blurs and quantum mottles. IEICE Trans (1976-1990). 1990;73(5):670–8.
27. Li Y, Lu J, Wang L, Yahagi T, Okamoto T. Removing noise from radiological image using multineural network filter. In: 2005 IEEE International Conference on Industrial Technology 2005. p. 1365–1370. https://doi.org/10.1109/ICIT.2005.1600848.
28. Li Y, Lu J, Wang L, Li S, Fan Y, Yahagi T. Removing noise from medical CR image using multineural network filter based on noise intensity distribution. In: Third International Conference on Natural Computation (ICNC 2007) (Vol. 3). 2007. p. 343-347. https://doi.org/10.1109/ICNC.2007.605.
29. Ikuta A, Ohta M, Kodera Y, Fujita M, Wada T. An improved stochastic restoration method using digital filter for medical X-ray images contaminated by quantum mottles. Med Imaging Tech. 1995;13(1):85–98.
30. Park C, Choo KS, Jung Y, Jeong HS, Hwang JY, Yun MS. CT iterative vs deep learning reconstruction: comparison of noise and sharpness. Eur Radiol. 2021;31(5):3156–64. https://doi.org/10.1007/s00330-020-07358-8.
31. Park C, Choo KS, Kim JH, Nam KJ, Lee JW, Kim JY. Image quality and radiation dose in CT venography using model-based iterative reconstruction at 80 kVp versus adaptive statistical iterative reconstruction-V at 70 kVp. Korean J Radiol. 2019;20(7):1167–75. https://doi.org/10.3348/kjr.2018.0897.
32. Kalisz K, Buethe J, Saboo SS, Abbara S, Halliburton S, Rajiah P. Artifacts at cardiac CT: physics and solutions. Radiographics. 2016;36(7):2064–83. https://doi.org/10.1148/rg.2016160079.
33. Song JS, Lee JM, Sohn JY, Yoon JH, Han JK, Choi BI. Hybrid iterative reconstruction technique for liver CT scans for image noise reduction and image quality improvement: evaluation of the optimal iterative reconstruction strengths. Radiol Med (Torino). 2015;120(3):259–67. https://doi.org/10.1007/s11547-014-0441-9.
34. Muhammad NA, Karim MK, Harun HH, Rahman MA, Azlan RN, Sumardi NF. The impact of tube current and iterative reconstruction algorithm on dose and image quality of infant CT head examination. Radiat Phys Chem. 2022:110272.https://doi.org/10.1016/j.radphyschem.2022.110272.
35. Lee YJ, Hwang JY, Ryu H, Kim TU, Kim YW, Park JH, Choo KS, Nam KJ, Roh J. Image quality and diagnostic accuracy of reduced-dose computed tomography enterography with model-based iterative reconstruction in pediatric Crohn's disease patients. Sci Rep. 2022;12(1):1. https://doi.org/10.1038/s41598-022-06246-z.

36. Chhetri S, Pendem S, Bharath JL. Low kilovoltage and low contrast volume neck CT protocol using iterative reconstruction techniques: a comparison with standard dose protocol. Radiat Phys Chem. 2022;193:109935. https://doi.org/10.1016/j.radphyschem.2021.109935.
37. Son W, Kim M, Hwang JY, Kim YW, Park C, Choo KS, Kim TU, Jang JY. Comparison of a deep learning-based reconstruction algorithm with filtered back projection and iterative reconstruction algorithms for pediatric abdominopelvic CT. Korean J Radiol. 2022;23(7):752. https://doi.org/10.3348/kjr.2021.0466.
38. Brady SL, Trout AT, Somasundaram E, Anton CG, Li Y, Dillman JR. Improving image quality and reducing radiation dose for pediatric CT by using deep learning reconstruction. Radiology. 2021;298(1):180–8. https://doi.org/10.1148/radiol.2020202317.
39. Zhang A, Jiang H, Ma L, Liu Y, Yang X. A Shearlet-based algorithm for quantum noise removal in low-dose CT images. In: Medical Imaging 2016: Image Processing (Vol. 9784). SPIE. 2016. p. 972-978. https://doi.org/10.1117/12.2216562.
40. Liu F, Chen G, Feng J, Yap PT, Shen D. Gaussianization of diffusion MRI magnitude data using spatially adaptive phase correction. Proc Int Soc Magnet Resonn Med. 2019;27:4609. https://doi.org/10.13140/RG.2.2.34492.51846.
41. Dar SU, Öztürk Ş, Korkmaz Y, Elmas G, Özbey M, Güngör A, Çukur T. Adaptive diffusion priors for accelerated MRI reconstruction. arXiv preprint arXiv:2207.05876. 2022. https://doi.org/10.48550/arXiv.2207.05876.
42. Srivastava A, Bhateja V, Tiwari H, and Satapathy SC. Restoration algorithm for Gaussian corrupted MRI using non-local averaging. In: Information Systems Design and Intelligent Applications. New Delhi: Springer. 2015. p. 831-840. https://doi.org/10.1007/978-81-322-2247-7_84.
43. Wu ZQ, Ware JA, Jiang J. Wavelet-based Rayleigh background removal in MRI. Electron Lett. 2003;39(7):1. https://doi.org/10.1049/el:20030396.
44. Yadav RB, Srivastava S, Srivastava R. Identification and removal of different noise patterns by measuring SNR value in magnetic resonance images. In: 2016 Ninth International Conference on Contemporary Computing (IC3). IEEE; 2016. p. 1-5. https://doi.org/10.1109/IC3.2016.7880212.
45. Lysaker M, Lundervold A, Tai XC. Noise removal using fourth-order partial differential equation with applications to medical magnetic resonance images in space and time. IEEE Trans Image Process. 2003;12(12):1579–90. https://doi.org/10.1109/TIP.2003.819229.
46. Martin-Fernandez M, Villullas S. The EM method in a probabilistic wavelet-based MRI denoising. Comput Math Methods Med. 2015;2015:182659. https://doi.org/10.1155/2015/182659.
47. Pal C, Das P, Chakrabarti A, Ghosh R. Rician noise removal in magnitude MRI images using efficient anisotropic diffusion filtering. Int J Imaging Syst Technol. 2017;27(3):248–64. https://doi.org/10.1002/ima.22230.
48. Aarya I, Jiang D, Gale T. Adaptive SNR filtering technique for Rician noise denoising in MRI. In: The 6th 2013 Biomedical Engineering International Conference. IEEE; 2013. p. 1-5. https://doi.org/10.1109/BMEiCon.2013.6687669.
49. Rabbani H. Statistical modeling of low SNR magnetic resonance images in wavelet domain using Laplacian prior and two-sided Rayleigh noise for visual quality improvement. In: 2008 International Conference on Information Technology and Applications in Biomedicine. IEEE; 2008. p. 116-119. https://doi.org/10.1109/ITAB.2008.4570560.
50. Narasimha C, Rao AN. An effective tumor detection approach using denoised MRI based on fuzzy bayesian segmentation approach. Int J Speech Technol. 2021;24(2):259–80. https://doi.org/10.1007/s10772-020-09782-z.
51. Fahmy AS. Background noise removal in cardiac magnetic resonance images using Bayes classifier. In: 2008 30th Annual International Conference of the IEEE Engineering in Medicine and Biology Society. IEEE; 2008. p. 3393-3396. https://doi.org/10.1109/IEMBS.2008.4649934.
52. Smith TB. MRI artifacts and correction strategies. Imaging Med. 2010;2(4):445. https://doi.org/10.2217/iim.10.33.
53. Wadghiri YZ, Johnson G, Turnbull DH. Sensitivity and performance time in MRI dephasing artifact reduction methods. Magn Reson Med. 2001;45(3):470–6. https://doi.org/10.1002/1522-2594.
54. Koay CG, Özarslan E, Basser PJ. A signal transformational framework for breaking the noise floor and its applications in MRI. J Magn Reson. 2009;197(2):108–19. https://doi.org/10.1016/j.jmr.2008.11.015.
55. Zhu Y, Shen W, Cheng F, Jin C, Cao G. Removal of high density Gaussian noise in compressed sensing MRI reconstruction through modified total variation image denoising method. Heliyon. 2020;6(3):e03680. https://doi.org/10.1016/j.heliyon.2020.e03680.
56. Virtue P, Lustig M. The empirical effect of Gaussian noise in undersampled MRI reconstruction. Tomography. 2017;3(4):211–21. https://doi.org/10.18383/j.tom.2017.00019.
57. Nowak RD. Wavelet-based Rician noise removal for magnetic resonance imaging. IEEE Trans Image Process. 1999;8(10):1408–19. https://doi.org/10.1109/83.791966.
58. Elaiyaraja G, Kumaratharan N, Chandra Sekhar Rao T. Fast and efficient filter using wavelet threshold for removal of Gaussian noise from MRI/CT scanned medical images/color video sequence. IETE J Res. 2022;68(1):10–22. https://doi.org/10.1080/03772063.2019.1579679.
59. Gregg RL, Nowak RD. Noise removal methods for high resolution MRI. In: 1997 IEEE Nuclear Science Symposium Conference Record (Vol. 2). IEEE; 1997. p. 1117-1121. https://doi.org/10.1109/NSSMIC.1997.670504.
60. Pizurica A, Wink AM, Vansteenkiste E, Philips W, Roerdink BJ. A review of wavelet denoising in MRI and ultrasound brain imaging. Curr Med Imaging. 2006;2(2):247–60. https://doi.org/10.2174/157340506776930665.
61. Amiri Golilarz N, Gao H, Kumar R, Ali L, Fu Y, Li C. Adaptive wavelet based MRI brain image de-noising. Front Neurosci. 2020;14:728. https://doi.org/10.3389/fnins.2020.00728.
62. Deepa B, Sumithra MG. Comparative analysis of noise removal techniques in MRI brain images. In: 2015 IEEE International Conference on Computational Intelligence and Computing Research (ICCIC). IEEE; 2015. p. 1–4. https://doi.org/10.1109/ICCIC.2015.7435737.
63. Reddy KS, Jaya T. De-noising and enhancement of MRI medical images using Gaussian filter and histogram equalization. Mater Today. 2021. https://doi.org/10.1016/j.matpr.2021.03.144.
64. Kumar N, Nachamai M. Noise removal and filtering techniques used in medical images. Orient J Comp Sci Technol. 2017;10(1):103–13. http://www.computerscijournal.org/pdf/vol10no1/OJCST_Vol10_N1_p_103-113.pdf.
65. Isa IS, Sulaiman SN, Mustapha M, Darus S. Evaluating denoising performances of fundamental filters for T2-weighted MRI images. Proc Comput Sci. 2015;60:760–8. https://doi.org/10.1016/j.procs.2015.08.231.
66. Rai HM, Chatterjee K. Hybrid adaptive algorithm based on wavelet transform and independent component analysis for denoising of MRI images. Measurement. 2019;144:72–82. https://doi.org/10.1016/j.measurement.2019.05.028.
67. Chalghoumi S, and Smiti A., Median filter for denoising MRI: Literature review. In: 2022 International Conference on Decision Aid Sciences and Applications (DASA). IEEE; 2022. p. 1603-1606. https://doi.org/10.1109/DASA54658.2022.9764981.
68. Ali HM. MRI medical image denoising by fundamental filters. High-Resolut Neuroimaging Basic Phys Princ Clin Appl. 2018;14:111–24. https://doi.org/10.5772/intechopen.72427.
69. Yan X, Zhou MX, Xu L, Liu W, Yang G. Noise removal of MRI data with edge enhancing. In: 5th International Conference on Bioinformatics and Biomedical Engineering. IEEE; 2011. p. 1-4. https://doi.org/10.1109/icbbe.2011.5780196.
70. Sahu S, Singh HV, Kumar B, Singh AK. A Bayesian multiresolution approach for noise removal in medical magnetic resonance images. J Intell Syst. 2020;29(1):189–201. https://doi.org/10.1515/jisys-2017-0402.
71. Manjón JV, Carbonell-Caballero J, Lull JJ, García-Martí G, Martí-Bonmatí L, Robles M. MRI denoising using non-local means. Med Image Anal. 2008;12(4):514–23. https://doi.org/10.1016/j.media.2008.02.004.
72. Sahu S, Anand A, Singh AK, Agrawal AK, Singh MP. MRI de-noising using improved unbiased NLM filter. J Ambient Intell Human Comput. 2022:1–2. https://doi.org/10.1007/s12652-021-03681-0.
73. Krissian K, Aja-Fernández S. Noise-driven anisotropic diffusion filtering of MRI. IEEE Trans Image Process. 2009;18(10):2265–74. https://doi.org/10.1109/TIP.2009.2025553.
74. Anand CS, Sahambi JS. MRI denoising using bilateral filter in redundant wavelet domain. In: TENCON 2008, 2008 IEEE Region 10 Conference. IEEE; 2008. p. 1-6. https://doi.org/10.1109/TENCON.2008.4766742.
75. Swetha MD, and Aditya CR. Sparse feature aware noise removal technique for brain multiple sclerosis lesions using magnetic resonance imaging. 2022;13(6):527–33. https://doi.org/10.14569/IJACSA.2022.0130664.

76. Zhang G, Huang C, Jiang J, Xu W, Chen J, Xu X. Denoising of brain magnetic resonance images using a MDB network. Multimedia Tools Applic. 2022:1–3. https://doi.org/10.1007/s11042-021-11521-8.
77. Alpar O, Dolezal R, Ryska P, Krejcar O. Nakagami-Fuzzy imaging framework for precise lesion segmentation in MRI. Pattern Recogn. 2022;128:108675. https://doi.org/10.1016/j.patcog.2022.108675.
78. Cong-Hua X, Jin-Yi C, Wen-Bin X. Medical image denoising by generalised Gaussian mixture modelling with edge information. IET Image Proc. 2014;8(8):464–76. https://doi.org/10.1049/iet-ipr.2013.0202.
79. Pham TD. Estimating parameters of optimal average and adaptive wiener filters for image restoration with sequential Gaussian simulation. IEEE Signal Process Lett. 2015;22(11):1950–4. https://doi.org/10.1109/LSP.2015.2448732.
80. Paris S, Hasinoff SW, Kautz J. Local laplacian filters: edge-aware image processing with a laplacian pyramid, ACM Trans. Graph. 2011;30(4):68. https://doi.org/10.1145/1964921.1964963.
81. Du J, Li W, Xiao B. Anatomical-functional image fusion by information of interest in local Laplacian filtering domain. IEEE Trans Image Process. 2017;26(12):5855–66. https://doi.org/10.1109/TIP.2017.2745202.
82. Yadav RB, Srivastava S, Srivastava R. A partial differential equation-based general framework adapted to Rayleigh's, Rician's and Gaussian's distributed noise for restoration and enhancement of magnetic resonance image. J Med Phys. 2016;41(4):254. https://doi.org/10.4103/0971-6203.195190.
83. Yadav RB. Design and implementation of filters for Restoration and Enhancement of Magnetic resonance images. 2017.
84. Morajab S, Mahdavi M. A non-local conventional approach for noise removal in 3D MRI. arXiv preprint arXiv:1608.06558. 2016. https://doi.org/10.48550/arXiv.1608.06558.
85. Soto ME, Pezoa JE, Torres SN. Thermal noise estimation and removal in MRI: a noise cancellation approach. In: Iberoamerican Congress on Pattern Recognition. Berlin, Heidelberg: Springer; 2011. p. 47-54. https://doi.org/10.1007/978-3-642-25085-9_5.
86. Khalilzadeh MM, Fatemizadeh E, Behnam H. Adaptive sparse representation for MRI noise removal. Biomed Eng. 2012;24(05):383–94. https://doi.org/10.4015/S1016237212500342.
87. Khan SU, Ullah N, Ahmed I, Chai WY, Khan A. MRI images enhancement using genetic programming based hybrid noise removal filter approach. Curr Med Imaging. 2018;14(6):867–73. https://doi.org/10.2174/1573405613666170619093021.
88. Baselice F, Ferraioli G, Pascazio V. A 3D MRI denoising algorithm based on Bayesian theory. Biomed Eng Online. 2017;16(1):1–9. https://doi.org/10.1186/s12938-017-0319-x.
89. Lui JK, Laprad AS, Parameswaran H, Sun YP, Albert MS, Lutchen KR. Statistically robust and semiautomatic quantification of ventilation from static hyperpolarized 3He MRI: application to asthma. InD28. Imaging obstructive lung diseases I. American Thoracic Society; 2009. p. A5580. https://doi.org/10.1164/ajrccm-conference.2009.179.1_MeetingAbstracts.A5580.
90. Dietrich O, Raya JG, Reeder SB, Ingrisch M, Reiser MF, Schoenberg SO. Influence of multichannel combination, parallel imaging and other reconstruction techniques on MRI noise characteristics. Magn Reson Imaging. 2008;26(6):754–62. https://doi.org/10.1016/j.mri.2008.02.001.
91. Sanches JM, Nascimento JC, Marques JS. An unified framework for Bayesian denoising for several medical and biological imaging modalities. In: 2007 29th Annual International Conference of the IEEE Engineering in Medicine and Biology Society. IEEE; 2007. p. 6267-6270. https://doi.org/10.1109/IEMBS.2007.4353788.
92. Upadhyay P, Upadhyay SK, Shukla KK. Magnetic resonance images denoising using a wavelet solution to laplace equation associated with a new variational model. Appl Math Comput. 2021;400:126083. https://doi.org/10.1016/j.amc.2021.126083.
93. Viswanath M, Seetharaman R, Nedumaran D. Adaptive mechanism for recognition of diseases in medical images. In: 2018 Tenth IEEE International Conference on Advanced Computing (ICoAC). 2018. p. 349–354. https://doi.org/10.1109/ICoAC44903.2018.8939059.
94. Viswanath M, Seetharaman R, Nedumaran D. Edge Detection in Medical Images–Smoothening Techniques. In: 2018 IEEE International Conference on Networking, Embedded and Wireless Systems (ICNEWS). 2018. p. 1–6. https://doi.org/10.1109/ICNEWS.2018.8903928.
95. Viswanath M, Seetharaman R, Nedumaran D. Medical Imaging-Boundary Solutions. In: 2019 Third IEEE International Conference on Inventive Systems and Control (ICISC). 2019. p. 605-608. https://doi.org/10.1109/ICISC44355.2019.9036469.
96. Viswanath M, Seetharaman R, Nedumaran D. Diffusion operandi gradient solutions. Caribbean J Sci. 2019;53(02):2505–11 http://caribjsci.com/gallery/is2.191.pdf.
97. Viswanath M, Seetharaman R, Nedumaran D. Electrical Impedance Tomography-Differential Solutions. In: 2019 IEEE 5th Global Electromagnetic Compatibility Conference (GEMCCON). 2019. p. 1–5. https://doi.org/10.1109/GEMCCON48223.2019.9132819.
98. Viswanath M, Seetharaman R, Nedumaran D. Medical portraiture–derivative methods and distributional solutions. In: IEEE 2019 11th International Conference on Advanced Computing (ICoAC). 2019. p. 259–264. https://doi.org/10.1109/ICoAC48765.2019.246850.
99. Natarajan BK. Sparse approximate solutions to linear systems. SIAM J Comput. 1995;24(2):227–34. https://doi.org/10.1137/S0097539792240406.
100. Wahba G. Practical approximate solutions to linear operator equations when the data are noisy. SIAM J Numer Anal. 1977;14(4):651–67. https://doi.org/10.1137/0714044.
101. Hazan E. Sparse approximate solutions to semi-definite programs, Latin American symposium on theoretical informatics. Berlin, Heidelberg: Springer. 2008. p. 306-316. https://doi.org/10.1007/978-3-540-78773-0_27.
102. Jing Z, Yanqing Z, Zhigang C, Jianhua L. Detecting boundary of salt dome in seismic data with edge-detection technique. SEG Technical Program Expanded Abstracts 2007. Society of Exploration Geophysicists; 2007. p. 1392-1396. https://doi.org/10.1190/1.2792759.
103. Garg B. An adaptive minimum-maximum value-based weighted median filter for removing high density salt and pepper noise in medical images. Int J Ad Hoc Ubiquitous Comput. 2020;35(2):84–95. https://doi.org/10.1504/IJAHUC.2020.109795.
104. Ilango G, Gowri BS. Neighbourhood median filters to remove speckle noise from CT–images. Int J Appl Inform Syst. 2012;04(10):40–6. https://doi.org/10.5120/ijais12-450829.
105. Abd Halim S, Wira NN, Hadi NA. Image denoising using modified diffusion functions on nonlinear second-order hyperbolic model. In: Journal of Physics: Conference Series (Vol. 1770, No. 1). IOP Publishing; 2021. p. 012043. https://doi.org/10.1088/1742-6596/1770/1/012043.
106. Rahimizadeh N, Hasanzadeh RP, Janabi-Sharifi F. An optimized non-local LMMSE approach for speckle noise reduction of medical ultrasound images. Multimedia Tools Applic. 2021;80(6):9231–53. https://doi.org/10.1007/s11042-020-10051-z.
107. Afshari P, Zakian C, Bachmann J, Ntziachristos V. Speckle reduction in ultrasound endoscopy using refraction based elevational angular compounding. Sci Rep. 2021;11(1):1–8. https://doi.org/10.1038/s41598-021-97717-2.
108. Khashman A, Dimililer K. Medical radiographs compression using neural networks and haar wavelet. In: IEEE EUROCON 2009. IEEE; 2009. p. 1448–1453. https://doi.org/10.1109/EURCON.2009.5167831.
109. Sivakumar R, Gayathri MK, Nedumaran D. Speckle filtering of ultrasound B-Scan Images - a comparative study between spatial and diffusion filters. In: 2010 IEEE Conference on Open Systems (ICOS 2010), 2010. p. 80–85, https://doi.org/10.1109/ICOS.2010.5720068.
110. Giusti SM, Ferrer A, Oliver J. Topological sensitivity analysis in heterogeneous anisotropic elasticity problem - theoretical and computational aspects. Comput Methods Appl Mech Eng. 2016;311:134–50. https://doi.org/10.1016/j.cma.2016.08.004.
111. Novotny AA, Feijóo RA, Taroco E, Padra C. Topological sensitivity analysis for three-dimensional linear elasticity problem. Comput Methods Appl Mech Eng. 2007;196(41–44):4354–64. https://doi.org/10.1016/j.cma.2007.05.006.
112. Viswanath M, Seetharaman R, Nedumaran D. Techniques for improvement of Medical Images. In: 2017 IEEE International Conference on Circuits and Systems (ICCS). 2017. p. 202-205. https://doi.org/10.1109/ICCS1.2017.8325990.
113. Azegami H, Shimoda M, Katamine E, Wu ZC. A domain optimization technique for elliptic boundary value problems. WIT Trans Built Environ. 1970;14. https://doi.org/10.2495/OP950071.

114. Tay WB, Tseng YH, Lin LY, Tseng WY. Towards patient-specific cardiovascular modeling system using the immersed boundary technique. Biomed Eng Online. 2011;10(1):1–7. https://doi.org/10.1186/1475-925X-10-52.
115. Bendsøe MP, Rodrigues HC. Integrated topology and boundary shape optimization of 2-D solids. Comput Methods Appl Mech Eng. 1991;87(1):15–34. https://doi.org/10.1016/0045-7825(91)90144-U.
116. Bogomolny A. Fundamental solutions method for elliptic boundary value problems. SIAM J Numer Anal. 1985;22(4):644–69. https://doi.org/10.1137/0722040.
117. Mathon R, Johnston RL. The approximate solution of elliptic boundary-value problems by fundamental solutions. SIAM J Numer Anal. 1977;14(4):638–50. https://doi.org/10.1137/0714043.
118. Amann H, Moser J. On the existence of positive solutions of nonlinear elliptic boundary value problems. Indiana Univ Math J. 1971;21(2):125–46 https://www.jstor.org/stable/24890168.
119. Gossez JP. Nonlinear elliptic boundary value problems for equations with rapidly (or slowly) increasing coefficients. Trans Am Math Soc. 1974;190:163–205. https://doi.org/10.1090/S0002-9947-1974-0342854-2.
120. Browder FE. Estimates and existence theorems for elliptic boundary value problems. Proc Natl Acad Sci. 1959;45(3):365–72. https://doi.org/10.1073/pnas.45.3.365.
121. Singh R, Reddy KS, Mathur T. Tracheobronchial carcinoid tumour causing a complete collapse of the one and compensatory hypertrophy of the other lung, resulting in a post-pneumonectomy-like syndrome. BMJ Case Reports CP. 2022;15(5):e250070. https://doi.org/10.1136/bcr-2022-250070.
122. Amann H, Hess PA. Multiplicity result for a class of elliptic boundary value problems. Proc Royal Soc Edinburgh Section A Math. 1979;84(1–2):145–51. https://doi.org/10.1017/S0308210500017017.
123. Starius G. Composite mesh difference methods for elliptic boundary value problems. Numer Math. 1977;28(2):243–58. https://doi.org/10.1007/BF01394455.
124. Singh R, Reddy KS, Mathur T. Tracheobronchial carcinoid tumour causing a complete collapse of the one and compensatory hypertrophy of the other lung resulting in a postpneumonectomy-like syndrome. BMJ Case Rep CP. 2022;15(5):e250070. https://doi.org/10.1136/bcr-2022-250070.
125. Shyu CR, Brodley CE, Kak AC, Kosaka A, Aisen AM, Broderick LS. ASSERT: A physician-in-the-loop content-based retrieval system for HRCT image databases. Comput Vis Image Underst. 1999;75(1–2):111–32. https://doi.org/10.1006/cviu.1999.0768.
126. Ceylan S, Ilbay K, Kuzeyli K, Kalelïoğlu M, Aktürk F, Özoran Y. Intraventricular meningioma of the fourth ventricle. Clin Neurol Neurosurg. 1992;94(2):181–4. https://doi.org/10.1016/0303-8467(92)90080-M.
127. Criscuolo GR, Symon L. Intraventricular meningioma. Acta Neurochir. 1986;83(3):83–91. https://doi.org/10.1007/BF01402383.
128. Kirsch CF. Imaging of midfacial and orbital trauma. Atlas Emerg Imaging Head-to-Toe. 2022:1–4. https://doi.org/10.1007/978-3-030-44092-3_7-1.
129. Sung EK, Nadgir RN, Fujita A, Siegel C, Ghafouri RH, Traband A, Sakai O. Injuries of the globe: what can the radiologist offer? Radiographics. 2014;34(3):764–76. https://doi.org/10.1148/rg.343135120.
130. Akkan K, Ucar M, Kilic K, Celtikci E, Ilgit E, Onal B. Unfused or twig-like middle cerebral artery. Eur J Radiol. 2015;84(10):2013–8. https://doi.org/10.1016/j.ejrad.2015.06.012.
131. Liu HM, Lai DM, Tu YK, Wang YH. Aneurysms in twig-like middle cerebral artery. Cerebrovasc Dis. 2005;20(1):1–5. https://doi.org/10.1159/000086119.
132. Goto Y, Nanto M, Oka H, Murakami N, Nakagawa T, Kimura S, Iwamoto Y, Inoue Y, Matsumoto K, Miyamoto J, Hashimoto N. Radiological and clinical features of twig-like middle cerebral artery in comparison with moyamoya angiopathy: a multicenter retrospective study. J Neurosurg. 2022;1(aop):1–9. https://doi.org/10.3171/2022.2.JNS212338.
133. Lansberg MG, Albers GW, Beaulieu C, Marks MP. Comparison of diffusion-weighted MRI and CT in acute stroke. Neurology. 2000;54(8):1557–61. https://doi.org/10.1212/WNL.54.8.1557.
134. Hacke W, Warach S. Diffusion-weighted MRI as an evolving standard of care in acute stroke. Neurology. 2000;54(8):1548–9. https://doi.org/10.1212/WNL.54.8.1548.
135. Ahn BJ, Kwon KY. Hemiballism after transient hemiparesis on the same side: a red flag of middle cerebral artery disease? Acta Neurol Belgica. 2022:1–3. https://doi.org/10.1007/s13760-022-01901-8.
136. Lee KY, Latour LL, Luby M, Hsia AW, Merino JG, Warach S. Distal hyperintense vessels on FLAIR: an MRI marker for collateral circulation in acute stroke? Neurology. 2009;72(13):1134–9. https://doi.org/10.1212/01.wnl.0000345360.80382.69.
137. Zhang M, Shi Q, Yue Y, Zhang M, Zhao L, Yan C. Evaluation of T2-FLAIR combined with ASL on the collateral circulation of acute ischemic stroke. Neurol Sci. 2022:1–0. https://doi.org/10.1007/s10072-022-06042-7.
138. Ahn SJ, Suh SH, Lee KY, Kim JH, Seo KD, Lee S. Hyperintense vessels on T2-PROPELLER-FLAIR in patients with acute MCA stroke: prediction of arterial stenosis and perfusion abnormality. Am J Neuroradiol. 2015;36(11):2042–7. https://doi.org/10.3174/ajnr.a4423.
139. Attenberger UI, Runge VM, Stemmer A, Williams KD, Naul LG, Michaely HJ, Schoenberg SO, Reiser MF, Wintersperger BJ. Diffusion weighted imaging: a comprehensive evaluation of a fast spin echo DWI sequence with BLADE (PROPELLER) k-space sampling at 3 T, using a 32-channel head coil in acute brain ischemia. Invest Radiol. 2009;44(10):656–61. https://doi.org/10.1097/rli.0b013e3181af3f0e.
140. Korkalainen N, Ilvesmäki T, Parkkola R, Perhomaa M, Mäkikallio K. Brain volumes and white matter microstructure in 8-to 10-year-old children born with fetal growth restriction. Pediatr Radiol. 2022:1–3. https://doi.org/10.1007/s00247-022-05372-0.
141. Omuro AM, Leite CC, Mokhtari K, Delattre JY. Pitfalls in the diagnosis of brain tumours. Lancet Neurol. 2006;5(11):937–48. https://doi.org/10.1016/s1474-4422(06)70597-x.
142. Razek AA. MR imaging of neoplastic and non-neoplastic lesions of the brain and spine in neurofibromatosis type I. Neurol Sci. 2018;39(5):821–7. https://doi.org/10.1007/s10072-018-3284-7.
143. Garg RK, Sinha MK. Multiple ring-enhancing lesions of the brain. J Postgrad Med. 2010;56(4):307–16. https://doi.org/10.4103/0022-3859.70939.
144. Haris M, Gupta RK, Singh A, Husain N, Husain M, Pandey CM, Srivastava C, Behari S, Rathore RK. Differentiation of infective from neoplastic brain lesions by dynamic contrast-enhanced MRI. Neuroradiology. 2008;50:531–40. https://doi.org/10.1007/s00234-008-0378-6.
145. Borba LA, Passos G, Oliveira I. Liquid biopsy and tumor DNA/RNA detection in the cerebrospinal fluid of patients diagnosed with central nervous system glioma–A review article. Surg Neurol Int. 2023;14(183):1–6. https://doi.org/10.25259/SNI_52_2023.
146. Piperi C, Saurty-Seerunghen MS, Levidou G, Sepsa A, Trigka EA, Klonou A, Markouli M, Strepkos D, Spyropoulou A, Kanakoglou DS, Lakiotaki E. Glioma cells expressing high levels of ALDH5A1 exhibit enhanced migration transcriptional signature in patient tumors. Neurotherapeutics. 2023;20(3):881–95. https://doi.org/10.1007/s13311-023-01354-8.
147. Piperi C, Markouli M, Gargalionis AN, Papavassiliou KA, Papavassiliou AG. Deciphering glioma epitranscriptome: focus on RNA modifications. Oncogene. 2023;42(28):2197–206. https://doi.org/10.1038/s41388-023-02746-y.
148. Rodrigues AJ, Medress ZA, Sayadi J, Bhambhvani H, Falkson SR, Jokhai R, Han SS, Hong DS. Predictors of spine metastases at initial presentation of pediatric brain tumor patients: a single-institution study. Child's Nervous Syst. 2023;39(3):603–8. https://doi.org/10.1007/s00381-022-05702-5.
149. Cocito C, Martin B, Giantini-Larsen AM, Valcarce-Aspegren M, Souweidane MM, Szalontay L, Dahmane N, Greenfield JP. Leptomeningeal dissemination in pediatric brain tumors. Neoplasia. 2023;39:100898. https://doi.org/10.1016/j.neo.2023.100898.
150. Franzini A, Picozzi P, Lasio GB, Pessina F. Staged Gamma Knife radiosurgery for a rosette-forming glioneuronal tumor of the fourth ventricle: a case report. Child's Nerv Syst. 2023:1–4. https://doi.org/10.1007/s00381-023-06014-y.
151. Sultan H, Balafif F, Nazwar TA, Wardhana DW, Eri AM, Djaya S. Tumor surgery management prevalence of computed tomography, magnetic resonance imaging, and positron emission tomography in ependymoma screening apparatus: a review, Teikyo. Med J. 2023;46(1):7891–8.
152. Prebet T, Sun Z, Ketterling RP, Zeidan A, Greenberg P, Herman J, Juckett M, Smith MR, Malick L, Paietta E, Czader M. Azacitidine with or without Entinostat for the treatment of therapy-related myeloid neoplasm: further results of the E1905 North American Leukemia Intergroup study. Br J Haematol. 2016;172(3):384–91. https://doi.org/10.1111/bjh.13832.

153. Bui N, Kuo C, Brown NJ, Dzihic E, Gendreau J, Patel NA, Patel S, Koester SW, Singh R, Abraham ME, Mammis A. Staged open cranial surgery for primary intra-axial neoplasms: a systematic review. World Neurosurg. 2023;175:e167–73. https://doi.org/10.1016/j.wneu.2023.03.046.
154. Furlanetti L, Ballestero MF, de Oliveira RS. Surgical anatomy of the approaches to the brainstem surgical anatomy for Brainstem tumors approaches, brain anatomy and neurosurgical approaches: a practical, illustrated, easy-to-use guide. Cham: Springer International Publishing; 2023. 569–589. https://doi.org/10.1007/978-3-031-14820-0_30.
155. Maia RC, Junior HL, dos Santos Luciano MC, Fiorenza NG, Ferraz CP, de Azevedo OG, Junior E, Araujo Filho S, Sobrinho O. A brain neoplasm follow-up in a tertiary public hospital of northeast of Brazil: 2014–2016 data. 2023. p. 1–21. https://doi.org/10.21203/rs.3.rs-2773800/v1.
156. Di Cristofori A, Carone G, Rocca A, Rui CB, Trezza A, Carrabba G, Giussani C. Fluorescence and intraoperative ultrasound as surgical adjuncts for brain metastases resection: what do we know? A systematic review of the literature. Cancers. 2023;15(7):e3151. https://doi.org/10.1002/brb3.3151.

Publisher's Note

Springer Nature remains neutral with regard to jurisdictional claims in published maps and institutional affiliations.